FIRST-PRINCIPLES STUDY OF HYDROGEN STORAGE MATERIALS

A Thesis
Presented to
The Academic Faculty

by

Zhu Ma

In Partial Fulfillment
of the Requirements for the Degree
Doctor of Philosophy in the
School of Physics

Georgia Institute of Technology
April 2008

FIRST-PRINCIPLES STUDY OF HYDROGEN STORAGE MATERIALS

Approved by:

Professor Mei-Yin Chou, Advisor
School of Physics
Georgia Institute of Technology

Professor Ahmet Erbil
School of Physics
Georgia Institute of Technology

Professor Uzi Landman
School of Physics
Georgia Institute of Technology

Professor Xiao-Qian Wang
Department of Physics
Clark Atlanta University

Professor Phillip N. First
School of Physics
Georgia Institute of Technology

Date Approved: December 10, 2007

To my son

who was born on January 29th, 2008

ACKNOWLEDGEMENTS

I owe my sincere thanks to the following people:

First and foremost, I'm deeply indebted to my advisor, Professor Mei-Yin Chou, for her excellent supervision throughout my PhD study. Ever since I entered the group, she has been an inspirational example for me not only for her intelligence, experience, and insight, but also for her passion and diligence in work. I could not have reached this point without her tonic advices and patient guidance during each stage of my thesis work.

I would also like to thank Dr. Amra Peles and Dr. Xin-Yuan Zhao for the help they provided during the last few years. Amra helped me in co-working on the sodium alanates after which I continued to work on my first project. Dr. Xin-Yuan Zhao helped me to work with linux and other computational skills.

I thank Prof. Ahmet Erbil, Prof. Phillip First, Prof. Uzi Landman, and Dr. Xiao-Qian Wang for agreeing to be in my thesis defense committee. I thank Mrs. Judy Melton for proofreading and feedbacks on the writing of my thesis.

I thank Dr. Wolfgang Geist, Dr. Li Huang, Pei Lin, Dr. Alexis Nduwimana, Dr. Amra Peles, Dr. Wen-Ying Ruan , Dr. Yan Wang, Dr. Jia-An Yan, Lang Zeng, and Dr. Xin-Yuan Zhao with whom I shared an enjoyable group. Their stimulating discussions and friendly company make my experience here educational and fun.

There are so many other people in the department that I want to thank, but can not mention each of their names, who have helped me, from whom I've learned, and with whom I've shared so many fun memories.

Last but not least, I owe special thanks to Wei Kang, without whose love, help, and support I could not have gone so far.

TABLE OF CONTENTS

LIST OF TABLES

LIST OF FIGURES

SUMMARY

The current world rely mainly on fossil fuels and face impending danger of their depletion. Overexploitation of fossil fuels also puts increasing pressure on the environment. There is an urgent research need for alternative energy strategies that are both sustainable and clean. Hydrogen (as a synthetic fuel) is believed to be able to provide such a scheme due to its unique physical and chemical advantages in carrying energy. Researchers and engineers must solve various scientific and technical problems encountered in the production, storage, and utilization of hydrogen before turning this vision into a practical hydrogen economy.

In particular, the study for onboard hydrogen storage application has attracted significant interest in the past decade. Compared with stationary storage, storing hydrogen onboard vehicle puts far more stringent requirements on the material. A hydrogen-driven automobile should have driving range and refueling time similar to a conventional one. The total storage volume and weight per unit energy should be comparable to gasoline. Hydrogenation/dehydrogenation should happen around ambient pressure and temperature, and with decent kinetics. In addition, onboard application also requires reversible hydrogen storage.

We present a first principle investigation in Chapter 3 to study the possible alloy phases of sodium and lithium alanates. In 1997 Bogdanovic *et al.* discovered that hydrogen can be reversibly stored inside the solid-state sodium alanate $NaAlH_4$ in presence of Ti-related catalysts[22] with a theoretical 5.6% hydrogen capacity by weight. Here we consider partial substitution of sodium with lithium in this compound, which is expected to result in alloyed phases with better hydrogen capacity than the original

system while hopefully keeping its reversibility. Structural and energetic properties of alloy systems $Na_{1-x}Li_xAlH_4$ and $Na_{3(1-x)}Li_{3x}AlH_6$ are studied via phase interpolation and *ab initio* calculations within density functional theory. Initial structures are constructed by interpolation based on the knowledge of sodium and lithium alanates, and the natural connection between these two structures. Ultrasoft pseudopotentials and generalized gradient approximation are used. Total energy and force/stress are calculated in momentum space using plane waves, with all forces/stresses minimized. Alloy system $Na_{1-x}Li_xAlH_4$ is found to be meta-stable with small mixing energy < 5 KJ/mol which is comparable to room temperature thermal energy. The equilibrium structure undergoes transition from tetragonal structure to monoclinic structure between x= 0.25 and 0.5. Within each structure volume decreases with increasing x, which can be explained by the smaller ion size of Li than Na. Our results show that phase-separated state of sodium and lithium alanates is preferred, although at higher temperature the mixed phase can be stabilized by thermal energy. Alloy system $Na_{3(1-x)}Li_{3x}AlH_6$ is also studied, and Na_2LiAlH_6 is found to be stable in agreement with experimental findings.

The Li-Mg-N-H system has been identified as a promising hydrogen storage material due to its moderate operation conditions as well as high capacity and reversibility[48, 38, 50]. The ternary system of Li-N-H[34] can be distabilized by partial substitution of lithium with elements of greater electronegativity such as magnesium. The (de)hydrogenation reaction of the new system proceeds with plateau pressure of 30 *bar* at 200°C with a reversible storage capacity of about 5% by weight. By altering Mg:Li molar ratio, this system can be further optimized over properties such as capacity, kinetics, and reaction enthalpy, etc. Recently Rijssenbeek *et al*[55] reported that the mixed imide, $Li_2Mg(NH)_2$, has disordered cation or cation-vacancy arrangements at room temperature and above, where the compound undergoes progressive disordering of the cations and vacancies as temperature raises, and the exact positions of lithium

and magnesium cations are not determined. In Chapter 4, We investigate the crystal structure of $Li_2Mg(NH)_2$ using first-principles total-energy calculations within the density functional theory. The possible cation arrangement in α-$Li_2Mg(NH)_2$ is studied systematically. A series of low-energy ordered configurations is found with similar total energies indicating possible cation-disordered arrangement, in agreement with the experimental finding. Specific local orderings are found in the cation-vacancy arrangement, where Mg atoms prefer face-diagonal arrangements on "cubes" formed by tetrahedral interstitial sites of an *fcc* lattice, and arrange themselves in alternating face-diagonal directions on opposite faces of two adjacent cubes. These energetically preferable local orderings shed light on the experimental disordered structure models. Based on our calculations, a possible ordered structure at lower temperature is proposed for $Li_2Mg(NH)_2$. In addition, the reaction energetics is calculated which confirms the phase stability observed in experiment.

Hydrogenation-induced metal-nonmetal transition is recently found in the quaternary system $LaMg_2Ni$-H. The transition happens without major rearrangement of the metal host structure (atom shifts$<$0.7 Å) in contrast to the usual case in simple systems based on rare earths or magnesium. The metal-nonmetal transition is induced by charge transfer of conduction electrons into tetrahedral $[NiH_4]^{4-}$ complexes with a closed-shell electron configuration. The other hydrogen atoms are not associated with the complex, and remain to be simple saline-like hydride anions surrounded by magnesium and lanthanum atoms (which act as electron donors). The $LaMg_2Ni$-H system is a first example with the coexistence of two types of hydrogen atoms in the same system. Recently a similar metal-nonmetal transition is reported in a palladium system $LaMg_2Pd$-H, where the intermetallic $LaMg_2Pd$ absorbs hydrogen under mild conditions to form nonmetallic hydride $LaMg_2PdH_7$. The hydrogenation takes place in two steps through the intermediate low concentration hydride $LaMg_2PdH_3$, which has partially disordered structure with either of the two Wyckoff positions H1

or H2 occupied by hydrogen atoms. Unlike the nickel system, the hydrogenation of this system is partially reversible and therefore presents greater interest for applications. In Chapter 5 we perform a first-principles investigation within the density functional theory to study the structural, energetics, and bonding properties of the $LaMg_2Pd$-H system. Projector augmented wave method and generalized gradient approximation are used. The energetics of the $LaMg_2Pd$-H system is examined through total energy calculations. Band structure and density of states are calculated for intermetallic $LaMg_2Pd$, low concentration hydride $LaMg_2PdH_3$, and full hydrogenated $LaMg_2PdH_7$. Partial charge density for certain bands is calculated and compared for configurations of $LaMg_2PdH_3$ with a full H1 or H2 occupancy. Calculations on band structure reveal no band gap for $LaMg_2Pd$ and $LaMg_2PdH_3$, and a fundamental direct gap of 0.7 eV at Γ (GGA) for $LaMg_2PdH_7$. The real gap is estimated to be more than 1.0 eV. Our calculation shows that metal-nonmetal transition happens from low concentration $LaMg_2PdH_3$ to terminal $LaMg_2PdH_7$. For $LaMg_2PdH_3$, the configuration with a full H2 occupancy is 0.026 eV/f.u lower in energy than that with a full H1 occupancy, which can be explained by the ligand interaction of H2 with the nearest Pd. In terminal $LaMg_2PdH_7$, this interaction of Pd d and ligand H s within PdH_4 complex is further strengthened leading to even more dispersed Pd d spectrum toward lower energy range in PDOS plot, which eventually results in an energy gap, in agreement with the 18-el' full shell model of the $[PdH_4]^{4-}$ complex.

CHAPTER I

INTRODUCTION

Today, the lifestyles of mobility, prosperity, and daily comfort in modern society depend on a steady and reliable energy supply, most of which currently sources from fossil fuels. By no means should people take this energy security for granted. Scientists must waste no time to assess and find out alternative sources of energy that are both scientifically possible and technologically promising, i.e., new forms of energy source that are sustainable in time, environmentally acceptable, and economically competitive compared with the traditional forms of energy source.

1.1 Current Situation Of Energy Sources

In general, there are three categories of energy sources. The first is chemical energy from oxidizing a reduced substance such as a hydrocarbon (where the energy comes from breaking of chemical bonds), or photophysical energy from absorbing sunlight and generating heat or electricity (where the energy comes from part of an electronic volt). The second is nuclear reaction from fission of heavy nuclei or fusion of light nuclei where the energy is of order MeV per reaction. The third is thermomechanical energy including wind, water, and geological steam or hot water where the energy involved is of order meV.

Fossil fuels are hydrocarbons such as coal, oil and natural gas sourced from the organic remains of prehistoric organisms. As the world's main energy supply (Table 1), these traditional energy sources can be used straightforwardly in combustion process. They are relatively inexpensive and can be easily transported. However, fossil fuels are essentially non-renewable energy sources in the long-term. The geological processes which create fossil fuels take millions of years, so they cannot be regenerated

Table 1: World Total Energy Demand (Mtoe*)

Energy Source/Type	1971	2002	Change 1971-2002 (%)
Coal	1,407	2,389	1.7
Oil	2,413	3,676	1.4
Gas	892	2,190	2.9
Nuclear	29	892	11.6
Hydro	104	224	2.5
Biomass and waste	687	1,119	1.6
Other renewables	4	55	8.8
Total	5,536	10,345	2.0

(*toe: the amount of energy released by burning one tonne of crude oil($\sim$42 GJ).)

Source: Data from IEA, World Energy Outlook, International Energy Agency, Paris, France, 2004.

within the timescales of human race once they have been exhausted.

Global energy consumption has doubled over the past 30 years or so (Table 1). The consumption is mainly accounted for by fossil fuels due to industrialization in North America, Europe, and Japan. The world's energy need is expected to (at least) double within the next half century. Rapid increase in energy consumption will be seen in China and India (Table 2), where about one third of the world's population resides. Essentially, the current world depends solely on oil resources, which are expected to deplete in the very near future. By then the cost of finding and extracting new deposits will render them too expensive for everyday use. Overexploitation of fossil fuels is also believed to be responsible for signs of significant change in global climate shown in recent years. Extensive use of fossil fuels is the major cause of global warming and acid rain, and the extraction process can be very damaging to the landscape.

Demands for cleaner, sustainable new energy sources other than fossil fuels therefore pose urgency research needs toward a secure energy future.

Table 2: World Total Energy Demand (Mtoe, see Table 1): (1) North America including U.S.A.; (2) U.S.A.; (3) South and Central America; (4) Europe and Euro-Asia; (5) Middle East; (6) Africa; (7) Asia Pacific.

Region	2001	2002	2003	2004	Average Increase/ Year (%)	2004 Change Over 2003 (%)
(1)	2,681.5	2,721.1	2,741.3	2,784.4	1.3	1.6
(2)	2,256.3	2,289.1	2,298.7	2,331.6	1.1	1.4
(3)	452.	454.4	460.2	483.1	2.2	5.
(4)	2,855.5	2,851.5	2,908.	2,964.	1.3	1.9
(5)	413.2	438.7	454.2	481.9	5.3	6.1
(6)	280.	287.2	300.1	312.1	3.7	4.
(7)	2,497.	2,734.9	2,937.	3,198.8	8.6	8.9
World	9,179.3	9,487.9	9,800.8	10,224.4	3.7	4.3

Biomass not included. Source from BP Statistical Review of World Energy, 2006.

1.2 Hydrogen As Clean, Efficient, Renewable Energy Carrier

Energy can be stored in various forms such as mechanical energy of a flywheel, electric or magnetic field energy of capacitors or coils, chemical energy of fossil fuels, or nuclear energy in uranium or deuterium. The energy contained in chemical bonds comes from unpaired outer electrons (i.e., valence electrons) of an atom, which tend to be stabilized by electrons from other atoms.

The hydrogen atom, in which the electron is accompanied by only one proton, has the best ratio of valence electrons to protons (neutrons) in the periodic table. The energy gain per electron is therefore very high, rendering the hydrogen atom an ideal energy carrier. In addition, hydrogen is the most abundant element on Earth, although the majority of which is chemically bound in water.

Molecular hydrogen gas H_2 can be generated in different ways. For example, it can be produced using sunlight combined with photovoltaic cells and water electrolysis. The majority of hydrogen consumed nowadays (about 5×10^{10} kg per year worldwide) is however transformed from fossil fuels by reaction of -CH_2- chains with H_2O producing H_2 and CO_2. Hydrogen has especially high chemical energy per mass (142

$MJ.kg^{-1}$) compared with other fuels (47 $MJ.kg^{-1}$ for liquid hydrocarbons, for example). When burnt with oxygen, the only product is water vapour, making hydrogen gas an environment-friendly fuel. Due to these physical and chemical advantages, and the successful use of hydrogen fuel in space technology, scientists in general as well as some companies, governmental agencies, and financial institutions believe that hydrogen will be a globally important synthetic fuel in the near future.

In particular, many people consider hydrogen as the ideal fuel to replace petrol in automobiles because it is lightweight and abundant, and oxidizes into environmentally benign H_2O. There are basically two ways to run a vehicle on hydrogen. One is to burn a mixture of hydrogen with air in an internal combustion engine in which the energy transformation efficiency is limited by the thermal Carnot efficiency ($\sim$25%, slightly higher than that of a petrol-air mixture). The other is to burn hydrogen with oxygen electrochemically in a fuel cell and use the produced electricity to drive an electric engine. The efficiency of this process can reach up to 50%. As a matter of fact, automobile companies like BMW have already started to develop and test cars that run on hydrogen.

Along with the promising nature and exciting scenarios, there are many technical challenges that people face in order to put hydrogen to use as an energy-carrying medium. For one, there lacks an efficient way of hydrogen storage in practice. Traditional methods include compressed gaseous hydrogen storage (up to 200 *bar* with steel tanks, and 450 *bar* with carbon-fibre-reinforced tanks) and low temperature liquid hydrogen storage (below critical temperature of -241°C). High pressure tanks can contain only $\sim$4% hydrogen by mass when full, and 4 kg H_2 (corresponding to 400 km coverage for an electric engine car) thus compressed still occupies about 60 gallons of volume. Considering the cost of the tank material and the compression and pressure controlling (during release), this is obviously not very efficient. Besides, there is the potential risk associated with operation of the high-pressure combustible

gas. Economically, cost of cryotechniques used to condensate hydrogen into liquid and keep it at the low temperature makes liquid hydrogen storage not very attractive for everyday use, either.

1.3 Scientific Challenges And Fundamental Research Needs Of On-board Hydrogen Storage

Hydrogen storage onboard vehicles presents great challenge in particular. Transportation applications require compact, lightweight, responsive hydrogen storage. Basic research needs to identify new storage materials and answer a lot of performance and system related questions. What are the ways to optimize the operating conditions (release rate, temperature, and delivery pressure)? What are the requirements for hydrogen purity, reversibility, refueling rate, and life cycle of the host material? How to assess and address issues such as system stability, permeation hydrogen loss, safty, toxicity, and efficiency, etc? Last but not least, can we make on-board hydrogen storage cheap enough so that hydrogen fuel is affordable and competitive to conventional gasoline fuel?

Traditionally, hydrogen is stored in its pure form as compressed gas or cryogenic liquid in tanks. Gaseous and liguid forms of hydrogen storage are far from meeting the Department of Energy (DOE) targets of transportation storage for 2015. On the other hand storage in solid state compounds appears to offer more possibilities to meet these requirements. For example, many metal hydrides can be synthesized by direct solid-gas reaction. Under high hydrogen pressure, new metal hydride phases with high coordination numbers or high oxidation states of the metals (such as Sr_2MgH_6, FeH, and K_2PtH_6) can be stabilized. Some compounds of hydrogen with light elements such as lithium, sodium, magnesium, boron, aluminum, and nitrogen are found to contain a high percentage of hydrogen by mass/weight. However the performance of these compounds in practice is seriously limited by either their high temperatures needed to release hydrogen, limited reversibility or kinetics, or issues like impurity.

For example, $LiBH_4$ contains 18 mass% of hydrogen, but recharging requires special treatment which can not be easily carried out onboard vehicle. Usage of dopants such as $TiCl_3$ improves the hydrogen release rate of $NaAlH_4$, but at the expense of dramatic reduction of hydrogen capacity (from 7.5 to 3.7 weight% at 80°C). The detailed mechanism of the catalysis in this process is not clear. Some physical methods such as ball milling (which decreases particle size and increases surface area) can be used to enhance hydrogen release rate, the detailed mechanism of which again needs further clarification. New materials need to be "invented" since no single material available to date is found to meet all the requirements for practical hydrogen storage onboard vehicle.

Innovative basic research is required to look beyond the storage material currently known in order to find effective hydrogen storage materials with breakthrough performance. Fundamental factors that determine bond strength, desorption kinetics, and cycling degradation need to be sorted out. Exact evaluation of demands on storage (capacity, charge and discharge conditions, recycling lifetime, and cost, etc.) needs efforts from all disciplines of chemistry, physics, and materials science. Theory and modeling of chemical bonding and kinetics are able to reveal key factors controlling material performance, and provide important guidance in search of new materials and in modification of their performance. The search for viable hydrogen storage materials requires high-risk and high-payoff basic research, which incorporates a search for new materials, sophisticated probing techniques, and advanced theory and modeling of chemical/physical bonding and kinetics changing with composition and particle size.

For on-board hydrogen storage, the ideal bond strength is between covalent bonding and physisorption. Typical bonds formed by light elements with hydrogen are too strong to break down, and need to be weakened with suitable methods to improve both absorption and desorption kinetics. Surface barriers to hydrogen transport can

be decreased by alloying or the formation of surface phases. The details of the mobile species and the mechanism of diffusion process need to be studied. Nanostructuring is another useful tool for tuning bond strength, kinetics, and reaction temperatures and pressures. The role of nanosize and nanostructure in bonding and kinetics needs to be understood. Small amounts of transition metal elements are usually able to tune the lattice spacing, or alter chemical/physical properties of hydrogen storage compounds. Dopants can also tune the reversibility of storage materials in the range of temperature and pressure of interest, the mechanism of which again needs to be understood. Of the 2,000 hydrogen storage materials known, most have not been examined in doped or nano state.

Basic research in hydrogen storage needs to focus on understanding the fundamental principles governing bond strength, kinetics, absorption and desorption processes, and degradation caused by cycling. It is further required to apply these principles to tailor the performance of known storage materials, and to identify (or even design) new (class of) materials with properties modified to suit the transportation (or other) demands of hydrogen economy.

For on-board hydrogen storage in transportation application, special research efforts should be made to understand the structural, thermodynamic, physical, and chemical properties of light-metal hydrides such as $NaAlH_4$, $LiAlH_4$, $NaBH_4$, $LiBH_4$, LiH, BeH_2, Li-N-H, etc. Solvent-free synthetic approaches need to be developed and proper experimental techniques need to be explored. A good understanding is needed for problems like lifetime degradation, fundamental atomic processes in hydrogen absorption/desorption, role of surface and surface catalysts, role of hydrogen-induced mass transport on phase transformations, and thermophysical properties of potential hydrogen storage materials, etc.

1.3.1 Synthesis and measurement

Many methods can be used to synthesize various hydrides, including solid-gas reaction, solution methods, ball-milling, ion implantation, and electrochemical methods. Solid-gas reaction between hydrogen and metals, intermetallics, or mixture of binary hydrides and metals are used to synthesize many metal hydrides. Solution methods are traditionally used to synthesize complex metal hydrides. They often introduces impurities that are hard to get rid of, and in many cases the resulting hydride system does not have reversibility. It is however in some cases the only way of successful synthesis (for example the first complex transition metal hydride K_2ReH_9). Ball-milling in a hydrogen atmosphere is currently used to synthesize many hydrogen storage materials.

Usually to determine the hydrogen content, gravimetric or volumetric methods are used upon hydrogen absorption or desorption or water production during oxidization. Ball-milling yields samples in fine powders. The growth of single crystal is usually not practical. Techniques like electrical transport are not feasible due to low sample quality of multiphase powder. Neither do high-temperature methods apply due to low thermodynamical stability of hydrogen storage materials. These difficulties make X-ray absorption near-edge structure spectroscopy (XANES) and photoelectron spectroscopy (PES) hard to apply. The position of hydrogen atoms is hard to identify using X-ray diffraction due to small mass ratio of H relative to other elements in the periodic table. Hydrogen shows the most significant isotope effect of all elements. Therefore deuterides (with better coherent scattering) can be exploited to make the location of the hydrogen atoms easier. Neutron powder diffraction in combination with high resolution X-ray diffraction (synchrotron) is used in the structure determination. Inelastic neutron scattering (INS) is used to study interatomic interactions and locate hydrogen positions in low concentration hydrides. Nuclear magnetic resonance (NMR), infrared (IR), Raman, Mössbauer, and muon

spin rotation spectroscopy (μSR) are used to give information on local structures and coordinated hydrogen dynamics in materials.

1.3.2 Ionic, covalent, and interstitial metal hydrides

Depending on the relative electronegativities χ, hydrogen reacts with main group metals to form different kinds of hydrides. Hydrogen takes on an extra electron from alkaline metals to form hydride anion H^-. The resulting ionic hydrides have low mobility and fixed content of hydrogen due to electron localization around H^- and strong polarizability. They often have similar structures as (hydride fluoride analogy) or even form solid solution with the fluorides. Ionic hydrides are thermodynamically too stable for reversible hydrogen storage. Hydrogen reacts with group 4a/5a metals forming covalent hydrides MH_2/MH_3. Many 5a hydrides exist in molecular forms. In ternary hydrides of main group metals such as $NaAlH_4/Na_3AlH_6$, hydrogen covalently bonds with Al to form complex anions $[AlH_4]^-/[AlH_6]^{3-}$ which then interact ionically with Na^+. They are therefore called complex hydrides and will be discussed in the next subsection. The first report of hydrogen reaction with a metal appeared in 1866 when palladium was observed to absorb hydrogen up to 935 times of its own volume. Metal hydrides with transition metal components form so called interstitial hydrides where hydrogen atoms occupy tetrahedral or octahedral interstitial sites. Interstitial hydrides consist of relatively heavy elements and therefore have low hydrogen capacity by weight.

1.3.3 Complex hydrides

Different from simple metal/intermetallic hydrides where hydrogen atoms are encapsulated in metallic interstitial sites, complex hydrides are characteristic of complexes formed by several (1, 2, 4, or 6) hydrogen atoms surrounding some other atom (such as Al, B, or N). Light-elements complex hydrides have higher hydrogen coordination number than simple metal hydrides and lower metal mass weight than transition

metal hydrides, and therefore of high hydrogen capacity by weight. Co-existence of both covalent and ionic types of bonding adds flexibility in adjusting their thermal stability. Potentially it is possible to make complex, multicomponent hydrides by mixing of existing hydrides, which allows the synthesis of tailored materials with desired properties. Complex hydrides are among the most viable candidates for the onboard hydrogen storage application to provide both high hydrogen capacity and desirable release/absorption thermodynamics/kinetics. Fundamental research is required for understanding of various properties and hydrogenation-dehydrogenation mechanisms of stoichiometric complex hydrides and multicomponent complex hydrides, their synthesis and processing, and role of dopants and catalysts. Further research is required to find possible ways of improvement, including the effect of nanoscale crystaline on their properties.

1.3.4 Hydrides in nanophase structures

Many hydrides based on intermetallic compounds form nanophase granular structures upon charging and discharging of hydrogen. Hydrogen storage properties are strongly influenced as material size is reduced to the nanoscale (1∼100 nm). Nano scale materials can have unique properties that are different from their bulk counterparts. New synthesis techniques are able to make nanoscaled hydrogen storage materials with improved thermodynamics and kinetics during hydrogen take-up and release. Specific architectures are designed to yield desired properties. At the nanoscale, hydrogen diffusion rate is increased as the required diffusion length is minimized. The transport rate can also be influenced by change in the phonon modes. At the nanoscale, it is also possible to control various property parameters more independently. On the other hand, formation of nanostructures may increase the susceptibility to corrosion, and reduce system stability.

According to the way hydrogen is stored, nanoscale hydrogen storage materials

can be classified into two general categories. The first is atomic/dissociative hydrogen storage materials such as complex hydrides, where molecular hydrgogens dissociate into hydrogen atoms and bond with lattice of the storage medium. The second includes various nanostructured materials (nanotubes, nanohorns, etc.) with high surface area or microporosity that store hydrogen in molecular state via physisorption. Nanostructured materials with increased surface area and surface curvature exhibit increased ability of hydrogen absorption.

Nanoscale techiques provide the possibility of removing some of the current limitations in bulk complex hydrides, therefore rendering these materials attractive for hydrogen storage applications. For example, nanotechniques might provide reduced heats of adsorption/desorption, faster kinetics, and new surface states with better hydrogen mobility in presence of proper catalysts. Experimental methods need to be explored for manipulation of particle size by thermal management during charging-discharging cycles. Theory and modeling of manophase and particle-size effects may lead to fruitful research directions exploiting this degree of freedom to enhance hydrogen storage performance.

1.3.5 Dopants

A class of transition metal dopants can have significant catalytic effects on light-metal complex hydrides. They can change the thermal and kinetic properties of the storage system, increasing the reaction rate, lowering reaction temperature, altering equilibrium hydrogen pressure, or even enabling reversibility. For nondissociative materials, binding strength of hydrogen molecules to the surface can also be enhanced by adding proper dopants. Proper research efforts are needed to give fundamental understanding of the role of dopants/catalysts in these systems.

1.4 Role Of Computer Simulation In Research Effort Toward The Hydrogen Economy

Development of new materials for hydrogen storage poses many scientific and technical challenges. Fundamental research is needed to understand the atomic level interaction of hydrogen in these materials in order to tailor and improve material properties that will lead to efficient hydrogen storage. This requires integrated efforts from physics, chemistry, material science, and engineering, and close collaboration between experiment and theory. This collaboration should aim at understanding experimental data of structural, thermodynamic, physical, and chemical properties of hydrogen storage systems, and at design and synthesis of novel storage materials. The absorption energy, hence the thermodynamics, of the material can be tailored by manipulating the electronic and physical structures (i.e. lattice parameters and strains, grain structure, Fermi level, polarization, and charge distribution, etc.) of the material.

More and more quantum mechanical calculations are used to assess the nature of the chemical bonding and the site preferences of hydrogen atoms in hydrogen storage materials, and the energy barriers, diffusion paths, and catalyzing mechanisms during hydrogen takeup and release. Modeling and simulation can help in understanding the experimental data and easier identification of factors key to major improvements of hydrogen storage, and help guide further experiments. Computer simulation can be a powerful tool in characterizing the structure and hydrgoen storage/diffusion properties, and in understanding various structure-properties relationships.

CHAPTER II

THEORETICAL METHODS

In this chapter, we outline the main method employed in calculation of hydrogen storage materials.

Generally, all theories of material are derived from quantum mechanics. Suppose a system is composed of N electrons and M nuclei, where each nucleus has a positive charge $Z_\alpha e$ (α=1, 2,...,M). The Schrödinger equation is

$$i\hbar\frac{\partial}{\partial t}\Psi = \hat{H}\Psi, \tag{1}$$

with $\Psi(\mathbf{x}_1, \mathbf{x}_2,...,\mathbf{x}_N; \mathbf{X}_1, \mathbf{X}_2,...,\mathbf{X}_M)$ being the wave function of the many-body system, and

$$\hat{H} = \sum_{\alpha=1}^{M}\left(-\frac{1}{2m_\alpha}\nabla_\alpha^2\right) + \sum_{\alpha<\beta}^{M}\frac{Z_\alpha Z_\beta}{r_{\alpha,\beta}} + \sum_{j=1}^{N}\left(-\frac{1}{2}\nabla_j^2\right) + \sum_{j<k}^{N}\frac{1}{r_{j,k}} + \sum_{j,\alpha}^{N,M}\left(-\frac{Z_\alpha}{r_{j,\alpha}}\right) \tag{2}$$

the Hamiltonian operator (atomic units used). m_α is the mass of the nucleus α, and r is the distance between two particles in the system. ($\hbar$=1, e^2=1, m_e=1)

Since the mass of a nucleus is much larger than the mass of an electron, the motion of the nuclei is much slower than the motion of electrons. In many cases, especially when we focus on the electronic structure of the material in its condensed (liquid/crystalline) states, the motion of nuclei can be separated adiabatically from the motion of electrons. This is the essential idea of the Born-Oppenheimer/adiabatic approximation. After the separation, the remaining time-independent Hamiltonian for the electrons is

$$\hat{H} = \sum_{j=1}^{N}\left(-\frac{1}{2}\nabla_j^2\right) + \sum_{j<k}^{N}\frac{1}{r_{j,k}} + \sum_{j,\alpha}^{N,M}\left(-\frac{Z_\alpha}{r_{j,\alpha}}\right), \tag{3}$$

and the (reduced) electronic wave function is just a function of the electrons' positions (and spins), assuming "frozen" nuclear degrees of freedom.

Usually the Hamiltonian in Equation (3) is still complicated. To obtain a reasonable solution to Equation (3), further simplification is necessary. One of the important simplifications comes from statistical mechanics. At room temperature the number density of electrons in materials of condensed matter is in the order of 10^{22} electrons/cm^3. This high density guarantees that the electrons are highly degenerated fermions, and the properties of the material pertaining to its electronic structure are mainly determined by the ground state of the electrons.

Another simplification comes from the ingenious idea of Hohenberg and Kohn [5]. In 1964, they proposed to use the density of electrons, instead of the many-body wave function, as the basic variable. They also proved that the external field $v(\mathbf{r})$ is a unique functional of the electron density $n(\mathbf{r})$ within an additive constant, and that there is a universal functional of the electron density $F[n]$, which makes the minimum of the functional $E[n] = \int d\mathbf{r} v(\mathbf{r}) n(\mathbf{r}) + F[n(\mathbf{r})]$ equal to the ground state energy of the electrons for an arbitrary external field $v(\mathbf{r})$, provided that the number of electrons is conserved. These results, now known as the Hohenberg-Kohn theorem, constitute the first milestone of the modern density functional theory of electrons.

2.1 Density Functional Theory

The fundamental postulate of density functional theory [5] is that any property, F($\mathbf{r}$), of a system of many interaction particles is actually a functional, $F[n(\mathbf{r})]$, of the ground state density $n(\mathbf{r})$. A functional is a real-valued function on a vector space, usually of functions. In this case, the functional F is a function of the scalar function of position $n(\mathbf{r})$. The charge density function $n(\mathbf{r})$ itself carries all the information we need to know for the ground and excited states of the many-body system.

2.1.1 Hohenberg-Kohn theorem

The proof of the theorems is reproduced as follows. Consider a system of inhomogeneous interacting electron gas under the influence of external potential $v(\mathbf{r})$, with Hamiltonian $H = T + V + U$ (Equation (3)), with

$$T \equiv \frac{1}{2}\int \nabla\psi^*(\mathbf{r})\nabla\psi(\mathbf{r})d\mathbf{r} \tag{4}$$

$$V \equiv \int v(\mathbf{r})\psi^*(\mathbf{r})\psi(\mathbf{r})d\mathbf{r} \tag{5}$$

$$U = \frac{1}{2}\int \frac{1}{|\mathbf{r}-\mathbf{r}'|}\psi^*(\mathbf{r})\psi^*(\mathbf{r}')\psi(\mathbf{r}')\psi(\mathbf{r})d\mathbf{r}d\mathbf{r}', \tag{6}$$

where $\hat{T}$ is the kinetic energy, $\hat{U}$ is the interaction energy between electrons, and $\hat{V}$ is the potential energy of the electrons in an external field $v(\mathbf{r})$ (due to positively charged nuclei, for example). The electronic density in the ground state Ψ is denoted by

$$n(\mathbf{r}) \equiv (\Psi, \psi^*(\mathbf{r})\psi(\mathbf{r})\Psi), \tag{7}$$

which is a functional of $v(\mathbf{r})$. Conversely it can be shown by *reductio ad absurdum* that $v(\mathbf{r})$ is a unique functional of $n(\mathbf{r})$ apart from a trivial constant. Suppose $|\Phi\rangle$ and $|\Phi'\rangle$ are the ground states for different external potentials $v(\mathbf{r})$ and $v'(\mathbf{r})$, respectively, and both $|\Phi\rangle$ and $|\Phi'\rangle$ yield the same $n_0(\mathbf{r})$, with ground state energies $E = \langle\Phi|\, H\, |\Phi\rangle$ and $E' = \langle\Phi'|\, H'\, |\Phi'\rangle$. It follows from the minimal property of the ground state that

$$E < \langle\Phi'|\, H\, |\Phi'\rangle = \langle\Phi'|\, H' + V - V'\, |\Phi'\rangle < E' + \int d\mathbf{r}\,[v(\mathbf{r}) - v'(\mathbf{r})]\, n_0(\mathbf{r}), \tag{8}$$

and

$$E' < \langle\Phi|\, H'\, |\Phi\rangle = \langle\Phi|\, H + V' - V\, |\Phi\rangle < E + \int d\mathbf{r}\,[v'(\mathbf{r}) - v(\mathbf{r})]\, n_0(\mathbf{r}). \tag{9}$$

Adding Equation (8) and (9) leads to $E + E' < E' + E$. The apparent inconsistency suggests that $v(\mathbf{r})$ is a unique functional of $n(\mathbf{r})$ within an additive constant.

Since $v(\mathbf{r})$ fixes H, the full many-particle ground state Ψ, and therefore the kinetic and interaction energy, is a unique functional of $n(\mathbf{r})$. By defining a universal

functional

$$F[n(\mathbf{r})] \equiv (\Psi, (T+U)\Psi) \tag{10}$$

the energy functional

$$E_v[n] \equiv (\Psi, H\Psi) = \int v(\mathbf{r})n(\mathbf{r})d\mathbf{r} + F[n] \tag{11}$$

equals the ground-state energy for the correct $n(\mathbf{r})$, and has a minimum, given that the number of particles of the system $N[n] \equiv \int n(\mathbf{r})d\mathbf{r}$ is kept constant.

2.1.2 Kohn-Sham equation

Although simplifying the problem dramatically, the Hohenberg-Kohn theorem itself is still not an implementable scheme. If $F[n]$ were a known and simple function of n, solving for the ground state of interaction electrons in a given external potential field $v(\mathbf{r})$ would be easy, since it just requires the minimization of a functional of the three-dimensional density function. However the form of the universal functional $F[n]$ remains undetermined. A simple localized form of $F[n]$ was proposed soon by Kohn and Sham in 1965. They argued that $F[n]$ is composed of three parts as

$$F[n] = \frac{1}{2}\int\int d\mathbf{r}d\mathbf{r}'\frac{n(\mathbf{r})n(\mathbf{r}')}{|\mathbf{r}-\mathbf{r}'|} + T_s[n] + E_{xc}[n], \tag{12}$$

where the first term is the coulomb interaction; $T_s[n] = \frac{1}{2}\int \nabla_r \nabla_{r'} n_1(\mathbf{r},\mathbf{r}')|_{r=r'}d\mathbf{r}$ is the kinetic energy of a system of noninteracting particles with the same ground-state density; and $E_{xc}[n]$ is the exchange and correlation energy:

$$E_{xc}[n] = \frac{1}{2}\int \frac{n_2(\mathbf{r},\mathbf{r}';\mathbf{r},\mathbf{r}') - n_1(\mathbf{r},\mathbf{r})n_1(\mathbf{r}',\mathbf{r}')}{|\mathbf{r}-\mathbf{r}'|}d\mathbf{r}d\mathbf{r}', \tag{13}$$

where, analogous to the defination of density (Equation (7)), we have

$$n_1(\mathbf{r}_1,\mathbf{r}_2) \equiv (\Psi, \psi^*(\mathbf{r}_1)\psi(\mathbf{r}_2)\Psi) \tag{14}$$

$$n_2(\mathbf{r}_1,\mathbf{r}_2;\mathbf{r}_3,\mathbf{r}_4) \equiv (\Psi, \psi^*(\mathbf{r}_1)\psi^*(\mathbf{r}_2)\psi(\mathbf{r}_3)\psi(\mathbf{r}_4)\Psi) \tag{15}$$

If $n(\mathbf{r})$ varies sufficiently slowly or is of high density, it can be shown that

$$E_{xc}[n] \approx \int d\mathbf{r}\, n(\mathbf{r})\epsilon_{xc}(n(\mathbf{r})) \tag{16}$$

where $\epsilon_{xc}(n)$ is the exchange and correlation energy density of a homogeneous electron gas of density n. Equation (16) is called the local-density approximation (LDA).

The ground state of the electron system is the minimum of the functional $E[n]$ subject to the condition of a conserved total number of electrons $\delta N = \int d\mathbf{r}\delta n(\mathbf{r}) = 0$. Using variational principle this is expressed as

$$\delta E = \int d\mathbf{r}\delta n(\mathbf{r}) \left\{ \frac{\delta T_s[n]}{\delta n} + v(\mathbf{r}) + \int d\mathbf{r}' \frac{n(\mathbf{r}')}{|\mathbf{r}-\mathbf{r}'|} + \mu_{xc}(n(\mathbf{r})) \right\} = 0, \tag{17}$$

where

$$\mu_{xc}(n) = \frac{d(n\,\epsilon_{xc}(n))}{dn} \tag{18}$$

is the exchange and correlation part of the chemical potential of a homogeneous electron gas of density n.

Equation (17) can be interpreted as the ground state of a fictitious non-interacting electron gas in an effective external potential $v^{eff}(\mathbf{r}) = v(\mathbf{r}) + \int d\mathbf{r}' \frac{n(\mathbf{r}')}{|\mathbf{r}-\mathbf{r}'|} + \mu_{xc}(n(\mathbf{r}))$. Thus the original many-particle problem of interacting inhomogeneous electron gas in an external field $v(n)$ can be replaced by solving the equivalent Schödinger equation of independent particles in an effective potential $v^{eff}(\mathbf{r})$:

$$\left\{ -\frac{1}{2}\nabla^2 + v^{eff}(\mathbf{r}) \right\} \psi_i(\mathbf{r}) = \epsilon_i \psi_i(\mathbf{r}), \tag{19}$$

with the corresponding number density of electrons given by $n(\mathbf{r}) = \sum_{i=1}^{N} |\psi_i(\mathbf{r})|^2$, where N is the total number of electrons in the system. Equation (19), known as the Kohn-Sham equation, can be solved in a self-consistent manner. Starting from a trial density $n^{in}(\mathbf{r})$, one first constructs the effective one-particle potential $v^{eff}(\mathbf{r})$, then solves Equation (19) to obtain the eigen energies ϵ_i and eigen states $\psi_i(\mathbf{r})$, from which a new density $n^{out}(\mathbf{r})$ is obtained. Through a proper mixing procedure, a new input

density is constructed, and the process is repeated until self-consistency is achieved. Since the kinetic energy can now be solved from Equation (19), the total energy of the system is then expressed as

$$E = \sum_{i=1}^{N} \epsilon_i - \frac{1}{2} \int \int d\mathbf{r} d\mathbf{r}' \frac{n(\mathbf{r}) n(\mathbf{r}')}{|\mathbf{r} - \mathbf{r}'|} + \int d\mathbf{r}\, n(\mathbf{r}) \left[\epsilon_{xc}(n(\mathbf{r})) - \mu_{xc}(n(\mathbf{r})) \right]. \tag{20}$$

The function $\epsilon_{xc}(n)$ can be further divided into the exchange and the correlation terms as

$$\epsilon_{xc}(n) = \epsilon_x(n) + \epsilon_c(n), \tag{21}$$

where the exchange contribution $\epsilon_x(n)$ is calculated from the Dirac exchange-energy functional

$$\epsilon_x(n) = -\frac{3}{4} \left(\frac{3}{\pi} \right)^{1/3} n^{1/3}, \tag{22}$$

or is obtained from a Hartee-Fork style calculation; while the correlation contribution now often comes from fitting the results of Monte Carlo simulations.

In the frame of the Kohn-Sham equation, there are other ways to estimate the exchange-correlation functional E_{xc}. A common way is the so called generalized gradient approximation (GGA). In this method, E_{xc} is a functional of the local electron density and its gradient. Formally, it is expressed as

$$E_{xc} = E_{xc}[n; \nabla n], \tag{23}$$

and in practice there are various forms of GGA for different requirements, such as the Perdew-Becke form, the Perdew-Wang 86 form, and the Langreth-Mehl-Hu form, etc. By taking into account the generalized gradient corrections, the strong overbinding of isolated molecules by LDA is removed.

Despite the fictitious nature of the independent particle problem, people find Kohn-Sham scheme works surprisingly well for many real systems of interacting electrons. Structural properties of materials such as the lattice constant, the bulk modulus, and the cohesive energy can generally be determined to within a few percent

of the experimental values. Band gap values are systematically underestimated by Kohn-Sham methods, however, since the eigenvalues in the Kohn-Sham equation are not designed to be quasiparticle energies.

2.2 Solving Kohn-Sham Equation Numerically

There are two kinds of methods in calculation of the KS ground state: (1) Direct methods: direct determining the minimum of the KS total energy functional. The direct methods are based on the fact that the KS energy functional is minimal at the electronic ground state. (2) Self-consistency methods: iterative diagonalization of the KS Hamiltonian in combination with the charge density/potential mixing scheme. Mathematically the plane-wave-basis formalism is one of the most convenient choices for solving the KS equation in a periodic system. However, it is extremely inefficient to expand core states or the oscillatory core region of the valence states in terms of plane waves. In practice, the plane-wave basis is always used in combination with the pseodopotential approximation.

2.2.1 Pseudopotential formalism

The electron wavefunctions have complicated nodal structures near the ion cores. In the plane wave method, this means that in order to describe the wavefunctions to an acceptable accuracy, the necessary energy cutoff in the k space will be very high. Since on most occasions, only the electron wavefunctions outside the core area vary according to different chemical environments, and contribute to the physical and chemical properties of material, it is desirable to smoothen the nodes near the inert core area. Various pseudopotentials are formulated with the same general goal to replace the true atomic potential and reproduce the effects of the core electrons outside the core region in different chemical environments, while being adequately efficient for computational purposes.

In general, pseudopotentials can be divided into two categories. One is empirical

and the other is *ab initio*. The difference between these two kinds of pseudopotentials is in how the potential parameters are obtained. The parameters of empirical pseudopotentials are fitted from experimental data for particular materials. Its accuracy depends on the fitting process and its usage is therefore limited to the material the parameters come from. The *ab initio* pseudopotentials (employed in this thesis) on the other hand are constructed from the inner electronic states of atoms of a certain element, and are independent of any other information of a specific chemical system. The *ab initio* pseudopotentials are therefore more universal and with better transferability compared with the empirical ones.

The basic idea of the *ab initio* pseudopotential method is illustrated by the orthogonalized-plane-wave (OPW) concept [8, 9, 10, 11]. It can be shown that the energy levels of valence electrons in solids can be calculated from a weak net effective pseudopotential V_p, in which a major part of the large negative potential energy inside the atomic core region is canceled by the large positive kinetic energy of the valence electrons in the same region. The large positive kinetic energy comes from the strong oscillation of the valence electron wavefunctions in the core region enforced by the constraint that a valence state must be orthogonal to each state inside (Pauli principle). The original "nodal" wave equation

$$\mathrm{H}\,|\psi_v\rangle = (\mathrm{T} + \mathrm{V})\,|\psi_v\rangle = \mathrm{E}_v\,|\psi_v\rangle \tag{24}$$

is transformed into an equivalent pseudo wave equation

$$(\mathrm{H} + \mathrm{V}_R)\,|\phi_v\rangle = (\mathrm{T} + \mathrm{V} + \mathrm{V}_R)\,|\phi_v\rangle \equiv (\mathrm{T} + \mathrm{V}_{ps})\,|\phi_v\rangle = \mathrm{E}_v\,|\phi_v\rangle\,. \tag{25}$$

The weak/smooth net potential $(\mathrm{V} + \mathrm{V}_R)$, referred to as the pseudopotential V_{ps}, in the Phillips-Kleinman (PK) form, for example, is defined as

$$\mathrm{V}_{ps}^{PK} = \mathrm{V} + \sum_c (\mathrm{E}_v - \mathrm{E}_c)\,|\psi_c\rangle\,\langle\psi_c|\,, \tag{26}$$

where the cancellation is realized by adding to the original negative V the second repulsive term that comes from the orthogonal constraint. For the OPW form of

pseudopotentials, the pseudo wave function is still quite "hard core", and is proportional, but not equal, to the real wave function outside the core region.

Since in the pseudopotential model, the core is a "black box" from which the valence wave functions emanate with some logarithmic derivative, any core pseudopotential yielding that logarithmic derivative is a valid pseudopotential. Improvement therefore can be achieved by imposing the following conditions: (1) All-electron and pseudopotential valence eigenvalues must be equal; (2) All-electron and pseudopotential atomic wave functions are equal beyond a cutoff radius; (3) Charge enclosed within the sphere of cutoff radius for the all-electron atom and the pseudoatom must be equal; (4) Smooth pseudopotential valence wave functions. Through a Friedel Sum Rule, the charge-conserving feature is mapped into another important feature: the logarithmic derivatives of the real and pseudo wave functions and their first energy derivatives agree beyond the cutoff radius

$$-\frac{1}{2}\frac{\partial}{\partial\varepsilon}\frac{\partial}{\partial r}lnR(r,\varepsilon)\bigg|_{r=r_{cl}}^{\varepsilon=\varepsilon_l} = \frac{1}{r_{cl}^2R^2(r_{cl},\varepsilon_l)}\int_0^{r_{cl}} R^2(r,\varepsilon_l)r^2dr. \tag{27}$$

Pseudopotentials constructed in such a way are referred to as norm-conserving pseudopotentials. They are relatively soft-core and almost energy-independent, and the resulting ionic pseudopotentials can be transferred to different atomic environments. In practice, the Hamann-Schluter-Chiang scheme [12] starts with modeling the valence potentials, while the Troullier-Martin scheme [13] directly models the pseudo wave functions. Inside the cutoff radius, the radial part of the wave function is constructed as

$$R_l^{ps}(r) = r^l e^{p(r)}, \qquad \text{with} \quad p(r) = \sum_{n=0}^{6} c_{2n}r^{2n}. \tag{28}$$

The coefficients are then determined by equating the mth derivatives of pseudo and all-electron wave functions at the cutoff radius up to m=4.

Following the above procedure, each angular momentum component of the pseudo

wave function experiences a different pseudopotential

$$\hat{V}_l^{ion}(r) = \hat{V}_{local}^{ion}(r) + \sum_l \hat{V}^{semilocal} l(r) \hat{P}_l. \tag{29}$$

The semilocal part of the potential can be transformed into a completely nonlocal form [14]

$$\sum_l \hat{V}^{semilocal} l(r) \hat{P}_l \Rightarrow \sum_l \frac{\left| \hat{V}^{nonlocal} l(r) \Phi_l^0(r) \right\rangle \left\langle \hat{V}^{nonlocal} l(r) \Phi_l^0(r) \right|}{\langle \Phi_l^0(r) | \hat{V}^{nonlocal} l(r) | \Phi_l^0(r) \rangle} \tag{30}$$

such that in band calculations the number of integrals required by each angular momentum and each point in the Brillouin zone is reduced from n(n+1) to n, where n is the number of **G** vectors used in the calculation.

2.2.2 Ultra-soft pseudopotentials

Although the norm-conserving pseudopotentials can be used in many general solid-state calculations, their aplication is limited for systems containing first-row and transition-metal elements. The difficulty lies in the inefficiency to represent the highly localized p and d orbitals which are already nodeless. The pseudo wave function can be made more soft by pushing the cutoff radius outward, but the norm-conserving constraint leaves little room for any significant improvement in the procedure.

The ultrasoft pseudopotential is first proposed by Vanderbilt in 1990 [15, 16]. It has the form of a sum of a few separable terms, and becomes local and vanishes outside the core. The scattering properties and their energy derivatives are constructed to be correct at several energies spanning the range of occupied statas. The transferability can be improved systematically by increasing the number of such energies. The pseudopotential does not follow the norm-conservation constraint. Instead it is charge-state dependent and is involved in the self-consistent screening process. These features allow the cutoff radius to be increased without compromising transferability even for $2p$ and d orbitals.

The pseudopotential is constructed by introducing a generalized eigenvalue problem at an arbitrary energy ε_i. Consider an all-electron wavefunction $\psi_i(\mathbf{r})$ of certain angular momentum lm which satisfies the equation

$$(T + V_{AE}(\mathbf{r}) - \varepsilon_i)\,|\psi_i(\mathbf{r})\rangle = 0 \tag{31}$$

where i=$\{\varepsilon_i lm\}$, T=$-\frac{1}{2}\nabla^2$, and V_{AE} is the original reference screened all-electron potential. Suppose $|\phi_i(\mathbf{r})\rangle$ is the desired pseudo wave function. Cutoff radii r_{cl} and r_c^{loc} are chosen for the wave functions and local pseudopotentials, respectively, and a diagnostic radius R is chosen so that all pseudo- and all-electron quantities agree beyond R. A local wave function $|\chi_i\rangle$ can be defined as

$$|\chi_i\rangle = (\varepsilon_i - T - V_{loc})\,|\phi_i\rangle\,, \tag{32}$$

which vanishes beyond R where V_{AE}=V_{loc} and ϕ_i=ψ_i. The nonlocal pseudopotential operator is defined as

$$V_{NL} = \frac{|\chi_i\rangle\,\langle\chi_i|}{\langle\chi_i|\phi_i\rangle}. \tag{33}$$

It can be verified that

$$(T + V_{loc} + V_{NL})\,|\phi_i\rangle = \varepsilon_i\,|\phi_i\rangle\,. \tag{34}$$

Next, a generalized V_{NL} is constructed involving several (usually from 1 to 3) energy levels. The set of pseudo wave functions ϕ_i are constructed from the all-electron wave functions ψ_i as before, except now they have to satisfy the generalized norm-conserving condition

$$Q_{ij} \equiv \langle\psi_i\,|\psi_j\rangle_R - \langle\phi_i\,|\phi_j\rangle_R = 0. \tag{35}$$

A set of local wave functions are defined as

$$|\beta_i\rangle = \sum_j (B^{-1})_{ji}\,|\chi_j\rangle\,, \text{ where} \quad B_{ij} \equiv \langle\phi_i|\chi_j\rangle\,. \tag{36}$$

The $|\beta_i\rangle$ are dual to the $|\phi_i\rangle$, and the new nonlocal pseudopotential operator can be chosen as

$$V_{NL} = \sum_{i,j} B_{ij}\,|\beta_i\rangle\,\langle\beta_j|\,. \tag{37}$$

It can be verified that

$$(T + V_{loc} + V_{NL} - \varepsilon_i) |\phi_i\rangle = 0 \tag{38}$$

and that B_{ij} and V_{NL} are Hermitian when Q_{ij}=0. It is further shown that the generalized norm-conserving constraint Q_{ij}=0 is not necessary if a generalized eigenvalue formalism is adopted, where a nonlocal overlap operator is defined:

$$S = 1 + \sum_{i,j} Q_{ij} |\beta_i\rangle \langle\beta_j| \tag{39}$$

and the nonlocal pseudopotential is redefined as

$$V_{NL} = \sum_{i,j} D_{ij} |\beta_i\rangle \langle\beta_j| \text{ , where } \quad D_{ij} = B_{ij} + \varepsilon_j Q_{ij}. \tag{40}$$

With the above defination it can be shown that

$$\langle\phi_i| S |\phi_j\rangle_R = \langle\psi_i |\psi_j\rangle_R \tag{41}$$

and the pseudo wavefunction $|\phi_i\rangle$ is the solution of the gerenalized eigenvalue problem

$$(H - \varepsilon_i S) |\phi_i\rangle = 0, \tag{42}$$

where $H = T + V_{loc} + V_{NL}$ and S are Hermitian. Taking ε derivative of the above equation, it can be shown that the logarithmic derivatives of the all-electron and pseudo wave functions match each other in the usual way. The deficit of valence charge in the core region associated with a pseudo wave function needs to be restored. The solutions of Euquation (42) therefore must be normalized according to

$$\langle\phi_{n\mathbf{k}}| S |\phi_{n'\mathbf{k}}\rangle = \delta_{nn'}, \tag{43}$$

and the valence charge density is defined as

$$n_v(\mathbf{r}) = \sum_{n,\mathbf{k}} \phi^*_{n\mathbf{k}}(\mathbf{r})\phi_{n\mathbf{k}}(\mathbf{r}) + \sum_{i,j} \rho_{ij} Q_{ij}(\mathbf{r}) \tag{44}$$

with

$$\rho_{ij} = \sum_{n,\mathbf{k}} \langle\beta_i| \phi_{n\mathbf{k}} \rangle\langle \phi_{n\mathbf{k}} |\beta_j\rangle \,, \tag{45}$$

$$Q_{ij}(\mathbf{r}) = \psi_i^*(\mathbf{r})\psi_j(\mathbf{r}) - \phi_i^*(\mathbf{r})\phi_j(\mathbf{r}). \tag{46}$$

With definition (44) it can be shown that $\int d^3r n_v(\mathbf{r}) = N_v$ where N_v is the number of valence electrons in the unit cell.

2.2.3 Projector-augmented-plane-wave method

As mentioned above, the efficiency of the pseudopotential method is limited when applied to first-row elements or elements with d or f electrons. What's more, there are times when it is necessary to treat some semicore states as valence states, in which case the pseudopotentials become hard and less transferable. The projector-augmented-plane-wave method [17] generalizes both the pseudopotential method and the linear augmented-plane-wave (LAPW) method. It allows an easier treatment of first-row and transition-metal elements, and provides access to the full wave function.

In real materials, the wave function is fairly smooth in the bonding region, whereas it oscillates rapidly in the core region due to the large attractive potential of the nucleus. This is the main difficulty for electronic structure methods to describe the bonding region with accuracy as well as account for the large variations in the atomic core. The augmented -wave methods deal with this problem by dividing the wave function into two parts, i.e., a partial-wave expansion within an atom-centered sphere and envelope functions outside the spheres. The value and derivative of the two parts are then matched at the sphere radius.

Consider a transformation $\mathcal{T}$ that connects the Hilbert space of the real/oscillating valence wave functions $|\Psi\rangle$ and that of a set of smooth pseudo wave functions $|\tilde{\Psi}\rangle$ which is similar to the change of a Schrödinger picture to a Heisenberg one:

$$|\Psi\rangle = \mathcal{T}|\tilde{\Psi}\rangle = \left(1 + \sum_R \hat{\mathcal{T}}_R\right)|\tilde{\Psi}\rangle. \tag{47}$$

Each $\hat{\mathcal{T}}_R$ acts only within some augmentation region Ω_R enclosing one atom. All-electron and pseudo wave functions coincide outside the augmentation regions. Within

Ω_R,

$$|\phi_i\rangle = \left(1 + \hat{\mathcal{T}}_R\right)|\tilde{\phi}_i\rangle, \tag{48}$$

where $|\phi_i\rangle$ and $|\tilde{\phi}_i\rangle$ are the all-electron and pseudo partial wave functions, respectively, and $i = \{R, nlm\}$. The pseudo partial wave functions are smooth and complete inside Ω_R, and identical to the all-electron partial wave functions outside Ω_R. Inside Ω_R, the pseudo (therefore the all-electron) wave functions can be expanded in terms of the pseudo partial waves

$$|\tilde{\Psi}\rangle = \sum_i |\tilde{\phi}_i\rangle c_i, \quad |\Psi\rangle = \mathcal{T}|\tilde{\Psi}\rangle = \sum_i |\phi_i\rangle\, c_i \tag{49}$$

since $|\phi_i\rangle = \mathcal{T}|\tilde{\phi}_i\rangle$. Therefore

$$|\Psi\rangle = |\tilde{\Psi}\rangle - \sum_i |\tilde{\phi}_i\rangle c_i + \sum_i |\phi_i\rangle\, c_i. \tag{50}$$

Because of the linear nature of $\mathcal{T}$ the coefficients have the form

$$c_i = \langle\tilde{p}_i|\tilde{\Psi}\rangle, \tag{51}$$

where the fixed function $\langle\tilde{p}_i|$ (localized in Ω_R) is called projector function corresponding to the pseudo partial wave function $|\tilde{\phi}_i\rangle$, with

$$\sum_i |\tilde{\phi}_i\rangle\langle\tilde{p}_i| = \mathbf{1}, \quad \text{or} \quad \langle\tilde{p}_i|\tilde{\phi}_j\rangle = \delta_{ij}. \tag{52}$$

Now the transformation is written as

$$|\Psi\rangle = \mathcal{T}|\tilde{\Psi}\rangle = \left(1 + \sum_i \left(|\phi_i\rangle - |\tilde{\phi}_i\rangle\right)\langle\tilde{p}_i|\right)|\tilde{\Psi}\rangle. \tag{53}$$

For the all-electron partial wave functions, a natural choice is the solution of the radial Schrödinger equation for the isolated atom (that are orthogonalized to the core states). They are obtained by radially integrateing the atomic Schrödinger equations. Both the partial waves and the projectors are functions on a radial grid multiplied by spherical harmonics. The projectors are also transformed into the same representation

as the pseudo wave functions, i.e., the plane waves. The core states are decomposed in a similar way

$$|\Psi^c\rangle = |\tilde{\Psi}^c\rangle + |\phi^c\rangle - |\tilde{\phi^c}\rangle, \tag{54}$$

where compared with the valence states case, the projector function is simplified into the unity operator. With Equation (53), the transformation of local operators are straightforward:

$$\tilde{A} = \mathcal{T}^\dagger A \mathcal{T} = A + \sum_{i,j} |\tilde{p_i}\rangle \left(\langle \phi_i | A | \phi_j \rangle - \langle \tilde{\phi}_i | A | \tilde{\phi_j} \rangle \right) \langle \tilde{p_j} |. \tag{55}$$

For nonlocal operators the following term needs to be added

$$\begin{aligned} \Delta A &= \sum_i |\tilde{p_i}\rangle \left(\langle \phi_i | - \langle \tilde{\phi}_i | \right) A \left(1 - \sum_j |\tilde{\phi_j}\rangle \langle \tilde{p_j}| \right) \\ &\quad + \left(1 - |\tilde{p_j}\rangle \langle \tilde{\phi_j}| \right) A \left(|\phi_i\rangle - |\tilde{\phi_i}\rangle \right) \langle \tilde{p_i}|. \end{aligned} \tag{56}$$

When A cannot be easily evaluated (for example the Coulomb potential is singular at the nuclear site), a term of the following form can be added to Equation (55),

$$B - \sum_{i,j} |\tilde{p_i}\rangle \langle \tilde{\phi}_i | B | \tilde{\phi_j} \rangle \langle \tilde{p_j}|, \tag{57}$$

where B is an arbitrary operator localized in Ω_R. (For the Coulomb potential this is equivalent to constructing a new potential that is identical to the real potential outside and smooth inside Ω_R; and B is the difference between the two.) Now the expectation value of an operator is

$$\langle A \rangle = \sum_n f_n \langle \Psi_n | A | \Psi_n \rangle = \sum_n f_n \langle \tilde{\Psi}_n | \tilde{A} | \tilde{\Psi}_n \rangle. \tag{58}$$

The charge density $n(r)$ at a point r in space is the expectation value of the real-space projection operator $|r\rangle \langle r|$. Hence

$$n(r) = \tilde{n}(r) + n^1(r) - \tilde{n}^1(r), \tag{59}$$

where

$$\tilde{n}(r) = \sum_n f_n \langle \tilde{\Psi}_n | r \rangle \langle r | \tilde{\Psi}_n \rangle,$$

$$n^1(r) = \sum_{n,(i,j)} f_n \langle \tilde{\Psi}_n | \tilde{p_i} \rangle \langle \phi_i | r \rangle \langle r | \phi_j \rangle \langle \tilde{p_j} | \tilde{\Psi}_n \rangle,$$

and

$$\tilde{n}^1(r) = \sum_{n,(i,j)} f_n \langle \tilde{\Psi}_n | \tilde{p_i} \rangle \langle \tilde{\phi}_i | r \rangle \langle r | \tilde{\phi_j} \rangle \langle \tilde{p_j} | \tilde{\Psi}_n \rangle.$$

Similarly the total energy functional is

$$\begin{aligned} E &= \sum_n f_n \langle \Psi_n | -\frac{1}{2}\nabla^2 | \Psi_n \rangle \\ &\quad + \frac{1}{2}\int dr \int dr' \frac{\left(n+n^Z\right)\left(n+n^Z\right)}{|r-r'|} + \int dr n \epsilon_{xc}(n) \\ &= \tilde{E} + E^1 - \tilde{E}^1, \end{aligned} \tag{60}$$

where

$$\begin{aligned} \tilde{E} &= \sum_n f_n \langle \tilde{\Psi}_n | -\frac{1}{2}\nabla^2 | \tilde{\Psi}_n \rangle \\ &\quad + \frac{1}{2}\int dr \int dr' \frac{(\tilde{n}+\hat{n})(\tilde{n}+\hat{n})}{|r-r'|} + \int dr \tilde{n} \bar{v} \\ &\quad + \int dr \tilde{n} \epsilon_{xc}(\tilde{n}), \end{aligned}$$

$$\begin{aligned} E^1 &= \sum_{n,(i,j)} f_n \langle \tilde{\Psi}_n | \tilde{p_i} \rangle \langle \phi_i | -\frac{1}{2}\nabla^2 | \phi_j \rangle \langle \tilde{p_j} | \tilde{\Phi}_n \rangle \\ &\quad + \frac{1}{2}\int dr \int dr' \frac{\left(n^1+n^Z\right)\left(n^1+n^Z\right)}{|r-r'|} \\ &\quad + \int dr n^1 \epsilon_{xc}\left(n^1\right), \end{aligned}$$

$$\begin{aligned} \tilde{E}^1 &= \sum_{n,(i,j)} f_n \langle \tilde{\Psi}_n | \tilde{p_i} \rangle \langle \tilde{\phi}_i | -\frac{1}{2}\nabla^2 | \tilde{\phi_j} \rangle \langle \tilde{p_j} | \tilde{\Phi}_n \rangle \\ &\quad + \frac{1}{2}\int dr \int dr' \frac{(\tilde{n}^1+\hat{n})(\tilde{n}^1+\hat{n})}{|r-r'|} + \int dr \tilde{n}^1 \bar{v} \\ &\quad + \int dr \tilde{n}^1 \epsilon_{xc}\left(\tilde{n}^1\right), \end{aligned}$$

where $\bar{v}$ is an arbitrary potential localized in Ω_R which is used to minimize truncation errors, and $\hat{n}$ is referred to as compensation charge density.

2.3 Momentum-space Formalism For Total-energy Calculations

For material systems with translational symmetry, solving the Kohn-Sham equation in the momentum space is a convenient choice. The invention of the fast Fourier transform (FFT) makes this process more efficient numerically. Following the density functional formalism in pseudopotential framework, the total crystal energy, defined as total energy difference between the solids and isolated atoms, is

$$E_{total} = T + V + \int E_{xc}(\mathbf{r})d\mathbf{r} \tag{61}$$

where $T = \sum_i \psi_i^*(\mathbf{r})(-\nabla^2)\psi_i(\mathbf{r})d\mathbf{r}$ is the total kinetic energy, $\int E_{xc}(\mathbf{r})d\mathbf{r}$ is the density functional exchange-correlation contribution to the total energy, and

$$V = \sum_{i,\mu,l} \int \psi_i^*(\mathbf{r}) U_{ps,l}(\mathbf{r} - \mathbf{R}_\mu)\hat{P}_l\psi_i(\mathbf{r})d\mathbf{r} + \frac{1}{2}\int\int \frac{\rho(\mathbf{r})\rho(\mathbf{r}')}{|\mathbf{r} - \mathbf{r}'|}d\mathbf{r}d\mathbf{r}' + \frac{1}{2}\sum_{\substack{\mu,\nu \\ \mu\neq\nu}} \frac{Z^2}{|\mathbf{R}_\mu - \mathbf{R}_\nu|} \tag{62}$$

is the electrostatic potential energy (Rydberg units used). $\psi_i(\mathbf{r})$ is the pseudo wavefunction of the valence electron. Index i denotes both wavevector $\mathbf{k}_i$ and band index n, and runs over all occupied valence states. $\rho(\mathbf{r}) \equiv \sum_i \psi_i^*(\mathbf{r})\psi_i(\mathbf{r})$ is the pseudo valence electron density. $\mathbf{R}_\mu$ is the lattice vector, and Z valence of the ion (one kind of ion assumed for notational simplicity). The terms in Equation (62) represent the core-valence interaction energy, the valence electron-electron Coulomb energy, and the ion-ion lattice energy, respectively. From the minimal property of the ground state total energy, the corresponding independent electron Schödinger equation can be derived variationally:

$$\left(-\frac{\nabla^2}{2} + \sum_{\mu,l} U_{ps,l}(\mathbf{r} - \mathbf{R}_\mu)\hat{P}_l + \int \frac{\rho(\mathbf{r}')}{|\mathbf{r} - \mathbf{r}'|}d\mathbf{r}' + \mu_{xc}(\mathbf{r})\right)\psi_i(\mathbf{r}) = \epsilon_i\psi_i(\mathbf{r}) \tag{63}$$

where the exchange-correlation potential $\mu_{xc}(\mathbf{r}) \equiv \partial E_{xc}(\mathbf{r})/\partial\rho(\mathbf{r})$ can be formulated from knowledge of homogeneous electron gas using local density approximation, for example.

Calculating the total energy of Equation (61) requires evaluation of a large number of six-dimensional integrals for electron-electron interaction term. To avoid this difficulty, plane wave basis is used to expand each quantity in Equation (61). The usage of smooth Pseudopotentials permits rapid convergence of the plane-wave expansion. Given a wavevector $\mathbf{k}$ in the first Brillouin zone and a reciprocal lattice vector $\mathbf{G}$, the corresponding plane-wave component is

$$|\mathbf{k}+\mathbf{G}\rangle = \frac{1}{\Omega} e^{i(\mathbf{k}+\mathbf{G})\cdot\mathbf{r}} \tag{64}$$

where Ω denotes the total volume of the material. Let the momentum-space representations of the wavefucntion, the charge density, the interelectronic Coulomb potential, and the exchange-correlation potential be denoted by $\psi(\mathbf{k}_i+\mathbf{G})$, $\rho(\mathbf{G})$, $V_{Coul}(\mathbf{G})$, and $\mu_{xc}(\mathbf{G})$, respectively. From the Poisson equation the Coulomb repulsion energy becomes

$$\frac{1}{2}\int\int \frac{\rho(\mathbf{r})\rho(\mathbf{r}')}{|\mathbf{r}-\mathbf{r}'|} d\mathbf{r}d\mathbf{r}' = \frac{1}{4}\Omega\sum_{\mathbf{G}} V_{Coul}(\mathbf{G})\rho(\mathbf{G}), \quad V_{Coul}(\mathbf{G}) = \frac{8\pi\rho(\mathbf{G})}{G^2}. \tag{65}$$

By decomposing plane waves into spherical harmonics and Bessel functions and using the translational invariance, the pseudopotential energy is written as

$$\begin{aligned}
&\sum_{i,\mu,l}\int \psi_i^*(\mathbf{r}) U_{ps,l}(\mathbf{r}-\mathbf{R}_\mu)\hat{P}_l\psi_i(\mathbf{r})d\mathbf{r} \\
&= \Omega\sum_{i,l,\mathbf{G},\mathbf{G}'} \psi^*(\mathbf{k}_i+\mathbf{G})\psi(\mathbf{k}_i+\mathbf{G}')\sum_{\mu}\frac{e^{i(\mathbf{G}'-\mathbf{G})\cdot\mathbf{R}_\mu}}{N} \\
&\times \frac{1}{\Omega_{at}}\int e^{-i(\mathbf{k}_i+\mathbf{G})\cdot\mathbf{r}} U_{ps,l}(\mathbf{r})\hat{P}_l\, e^{i(\mathbf{k}_i+\mathbf{G}')\cdot\mathbf{r}} d\mathbf{r} \\
&= \Omega\sum_{i,l,\mathbf{G},\mathbf{G}'} \psi^*(\mathbf{k}_i+\mathbf{G})\psi(\mathbf{k}_i+\mathbf{G}')S(\mathbf{G}'-\mathbf{G})U_{ps,l,\mathbf{k}_i+\mathbf{G},\mathbf{k}_i+\mathbf{G}'},
\end{aligned} \tag{66}$$

where $\Omega_{at} = \frac{\Omega}{N}$. $S(\mathbf{G}'-\mathbf{G})$ is the structure factor. Assuming spherical symmetry of the ionic pseudopotenetial of the isolated atom, the generalised non-local form factor

is

$$\begin{aligned} U_{ps,l,\mathbf{k}_i+\mathbf{G},\mathbf{k}_i+\mathbf{G}'} &\equiv \frac{1}{\Omega_{at}} \int e^{-i(\mathbf{k}_i+\mathbf{G})\cdot\mathbf{r}} U_{ps,l}(\mathbf{r}) \hat{P}_l \, e^{i(\mathbf{k}_i+\mathbf{G}')\cdot\mathbf{r}} d\mathbf{r} \\ &= \frac{(2l+1)4\pi}{\Omega_{at}} \int U_{ps,l}(r) j_l(|\mathbf{k}_i+\mathbf{G}|r) j_l(|\mathbf{k}_i+\mathbf{G}'|r) \\ &\times \; r^2 dr P_l(cos\gamma) \end{aligned} \tag{67}$$

where j_l and P_l are spherical Bessel functions and Legengre polynomials, respectively, with $cos\gamma = \frac{(\mathbf{k}_i+\mathbf{G})\cdot(\mathbf{k}_i+\mathbf{G}')}{|\mathbf{k}_i+\mathbf{G}|\cdot|\mathbf{k}_i+\mathbf{G}'|}$. It is always convenient to decompose the pseudopotentials into pure local part and non-local parts, $\sum_l U_{ps,l}(\mathbf{r})\hat{P}_l = U_{ps}(\mathbf{r}) + \sum_l^{\infty} U'_{ps,l}(\mathbf{r})\hat{P}_l$ so that long-range interaction$\sim -\frac{2z}{r}$ will be taken care of by the local part, and the non-local parts will be of short range. For local pseudopotential, Equation (66) reduces to

$$\sum_{i,\mu} \int \psi_i^*(\mathbf{r}) U_{ps}(\mathbf{r}-\mathbf{R}_\mu)\psi_i(\mathbf{r}) d\mathbf{r} = \Omega \sum_{\mathbf{G}} S(\mathbf{G}) U_{ps}(\mathbf{G}) \rho(\mathbf{G}). \tag{68}$$

After this separation Equation (66) becomes

$$\begin{aligned} \sum_{i,\mu,l} \int \psi_i^*(\mathbf{r}) U_{ps,l}(\mathbf{r}-\mathbf{R}_\mu)\hat{P}_l\psi_i(\mathbf{r}) d\mathbf{r} = \Omega \Bigg(\sum_{\mathbf{G}} S(\mathbf{G})) U_{ps}(\mathbf{G})\rho(\mathbf{G}) \\ + \sum_{i,l,\mathbf{G},\mathbf{G}'} \psi^*(\mathbf{k}_i+\mathbf{G})\psi(\mathbf{k}_i+\mathbf{G}') S(\mathbf{G}'-\mathbf{G}) U'_{ps,l,\mathbf{k}_i+\mathbf{G},\mathbf{k}_i+\mathbf{G}'} \Bigg) \end{aligned} \tag{69}$$

The decomposition of Kohn-Sham equation (Equation (63)) in the plane-wave basis is

$$\begin{aligned} \sum_{\mathbf{G}'} \frac{1}{2}[(\mathbf{k}+\mathbf{G}')^2 \delta_{\mathbf{G}\mathbf{G}'} + \frac{1}{2} V_{coul}(\mathbf{G}'-\mathbf{G}) + \mu_{xc}(\mathbf{G}'-\mathbf{G}) + S(\mathbf{G}'-\mathbf{G}) \\ \times \; [U_{ps}(\mathbf{G}'-\mathbf{G}) + \sum_l U'_{ps,l,\mathbf{k}_i+\mathbf{G},\mathbf{k}_i+\mathbf{G}'}]]\psi(\mathbf{k}_i+\mathbf{G}') = \epsilon_i \psi(\mathbf{k}_i+\mathbf{G}). \end{aligned} \tag{70}$$

To further simplify the total energy expression, multiply the left side of Equation (63) by $\psi_i^*(\mathbf{r})$ and integrate over $\mathbf{r}$ and sum over i, and substitute the result into Equation

(61). We have

$$E_{total} = \sum_i \epsilon_i - \frac{1}{2}\int \frac{\rho(\mathbf{r})\rho(\mathbf{r}')}{|\mathbf{r}-\mathbf{r}'|} d\mathbf{r} d\mathbf{r}' - \frac{1}{4}\int \mu_{xc}(\mathbf{r})\rho(\mathbf{r}) d\mathbf{r} + \frac{1}{2}\sum_{\substack{\mu,\nu \\ \mu\neq\nu}} \frac{Z^2}{|\mathbf{R}_\mu - \mathbf{R}_\nu|}$$

$$= \sum_i \epsilon_i - \Omega\left[\frac{1}{4}\sum_{\mathbf{G}} V_{Coul}(\mathbf{G})\rho(\mathbf{G}) + \frac{1}{8}\sum_{\mathbf{G}} \mu_{xc}(\mathbf{G})\rho(\mathbf{G})\right] + \frac{1}{2}\sum_{\substack{\mu,\nu \\ \mu\neq\nu}} \frac{Z^2}{|\mathbf{R}_\mu - \mathbf{R}_\nu|} \quad (71)$$

2.4 The Vienna Ab-initio Simulation Package

The Vienna ab-initio simulation package (VASP) [20] is used for performing first-principles total-energy calculations within the density functional theory. It uses ultra-soft pseudopotentials or the projector-augmented wave method and a plane wave basis set. The corrected linear tetrahedron method is used to interpolate linearly between k points defining the corners of the tetrahedra when evaluating the band-structure energy. Partial occupancies are introduced at zero temperature as a tool to reduce the number of k points required to sample the Brillouin zone, especially for metallic systems. Smearing methods are introduced as a mathematical tool to improve the convergence with respect to the number of k points. The problem of solving for the Kohn-Sham ground state is split into two independent sub-problems: (1) The determination of the eigenfunctions and eigenvalues for a fixed charge density or potential; (2) Calculation of the self-consistent charge density or potential by proper mixing procedure and repeat of step (1). VASP uses efficient diagonalization, mixing, and force-prediction schemes to accelerate the solution process.

CHAPTER III

FIRST-PRINCIPLES INVESTIGATION OF SODIUM AND LITHIUM ALLOYED ALANATES

3.1 Alkali Alanates As Novel Hydrogen Storage Materials

Complex hydrides $M_x(AH_n)_y$ consist of a family of compounds, where M is one of the alkali or alkaline earth elements, A is Al or B, and n=4 or 6 corresponding to different degree of hydrogenation. $NaAlH_4$ and $LiAlH_4$ have attracted much interest in the past decade as promising on-board hydrogen storage materials [3]. The dehydrogenation/rehydrogenation chemical reaction proceeds in two steps, through the intermediate compound M_3AlH_6:

$$MAlH_4 \leftrightarrow \frac{1}{3}M_3AlH_6 + \frac{2}{3}Al + H_2 \quad (72)$$

$$\leftrightarrow MH + Al + \frac{3}{2}H_2, \quad (73)$$

where M stands for Na or Li. First the fully hydrogenated compound $MAlH_4$ decomposes into the partially hydrogenated compound M_3AlH_6 and the Al metal, releasing H_2; then the intermediated compound M_3AlH_6 furthur decomposes into alkali hydride MH and the Al metal, releasing more H_2. The reversibility, kinetics, temperature and pressure of this process can be improved by means such as doping or mechanical preprocessing. $LiAlH_4$ has 7.9 w% hydrogen capacity. The overall decomposition goes easily, but with poor reversibility for step (72). $NaAlH_4$ has total hydrogen capacity of 5.6% by weight. On the other hand, adding proper Ti-based catalysts can make decomposition of $NaAlH_4$ reversible.

In search of materials with optimal properties for transportation applications, current candidates need to be modified to have high hydrogen weight percentage (>

6.5%), high reversibility, moderate reaction temperature and pressure (preferably not too far from ambient condition), and good absorption/desorption kinetics [23, 6]. For $NaAlH_4$, partial substitution of Na with the lighter element Li is expected to result in alloyed phases with higher H w% than the pure sodium alanate while maintaining good reversibility.

In this work, we examine the possibility of finding alloyed complex hydrides of the form $Na_{1-x}Li_xAlH_4$ and $Na_{3(1-x)}Li_{3x}AlH_6$ via first-principles calculations. Section 4.2 gives details of the calculation. Results and discussions are presented in Section 3.3 and 3.4, respectively. In Section 3.3 we construct the initial geometry of the alloyed system from the known structures of the sodium and lithium alanates and compare the inital and the equilibrium structure for various compositions in Section 3.4. A transition from the tetragonal to the monoclinic structure is seen between x= 0.25 and x= 0.5. Alloying energy is estimated, and the phase stability of the alloyed systems is discussed. Section 3.5 summarizes our results.

3.2 Computational Details

The method we employ is a first-principles calculation within the density functional theory (DFT) [5], where the total energy and force/stress are calculated in momentum space with a plane-wave basis [58]. Calculations are done with the Vienna ab-initio simulation package (VASP) [20] using ultrasoft pseudopotentials [15]. The generalized gradient approximation (GGA) [18] is used for the exchange-correlation energy functional. A kinetic energy cutoff of 525 eV for the plane waves and a k-grid interval of ~ 0.2 Å^{-1} for the reciprocal space sampling are used so that total energy convergence is achieved. Our general procedure is to relax the forces and stresses under the constant-volume constraint, then let the system volume also evolve to minimize the force and stress. The force is considered minimized if any component on any atom is smaller than 0.02 eV/Å. We construct initial geometries of the Na-Li alloyed systems

Table 3: Calculated lattice parameters for several complex hydrides. Calculations are in good agreement with the experimental data (in parentheses) [26, 27, 28, 29, 30, 31]. Also listed is the volume per AlH_n (n=4 or 6) complex for each compound. $Mg(AlH_4)_2$ is included to show similar volume/AlH_4 to that of $NaAlH_4$ and $LiAlH_4$. Notice for $LiAlH_4$, calculation in tetragonal $I4_1/a$ structure shows big volume collapse compared with the monoclinic phase. Notice angle γ in Li_3AlH_6 corresponds to angle β in Na_3AlH_6. Z is the number of chemical units per unit cell.

Comp--ound	Space group	Z	Unit cell parameters a (Å)	b (Å)	c (Å)	α(°)	β(°)	γ(°)	vol./AlH_n (Å^3)
$NaAlH_4$	$I4_1/a$	4	4.984	= a	11.157	90.	90.	90.	69.3
			(4.9802)		(11.1482)				(69.1)
$LiAlH_4$	$I4_1/a$	4	4.585	= a	10.127	90.	90.	90.	53.2
	$P2_1/c$	4	4.812	7.742	7.795	90.	111.95	90.	67.3
			(4.8174)	(7.8020)	(7.8214)		(112.228)		(68.0)
$Mg(AlH_4)_2$	$P\bar{3}m1$	1	5.211	= a	6.000	90.	90.	120.	70.6
			(5.2084)		(5.8392)				(68.6)
Na_3AlH_6	$P2_1/n$	2	5.342	5.515	7.693	90.	90.16	90.	113.3
			(5.390)	(5.514)	(7.725)		(90.14)		(114.8)
Na_2LiAlH_6	$Fm\bar{3}m$	2	5.170	= a	7.312	90.	90.	90.	97.7
			(5.22187)		(7.38484)				(100.7)
Li_3AlH_6	$R\bar{3}$	2	5.564	= a	= a	88.63	= α	91.37	86.0
			(5.6365)			(88.55)		(91.45)	(89.4)

based on the known structures of the pure sodium and lithium alanates and search for equilibrium structures of the alloy systems starting from these initial constructions.

3.3 Structures Of The Alloy Systems $Na_{1-x}Li_xAlH_4$ And $Na_{3(1-x)}Li_{3x}AlH_6$

Figures 1 (a)-(e) show the ball-and-stick models for experimentally observed tetrahydrides $NaAlH_4$, $LiAlH_4$ and octahydrides Na_3AlH_6, Na_2LiAlH_6, and Li_3AlH_6. Al atoms (grey) are surrounded by ligand H atoms (white) forming complexes. Large (green) atoms are Na, and smaller (red) ones are Li. The common structural features

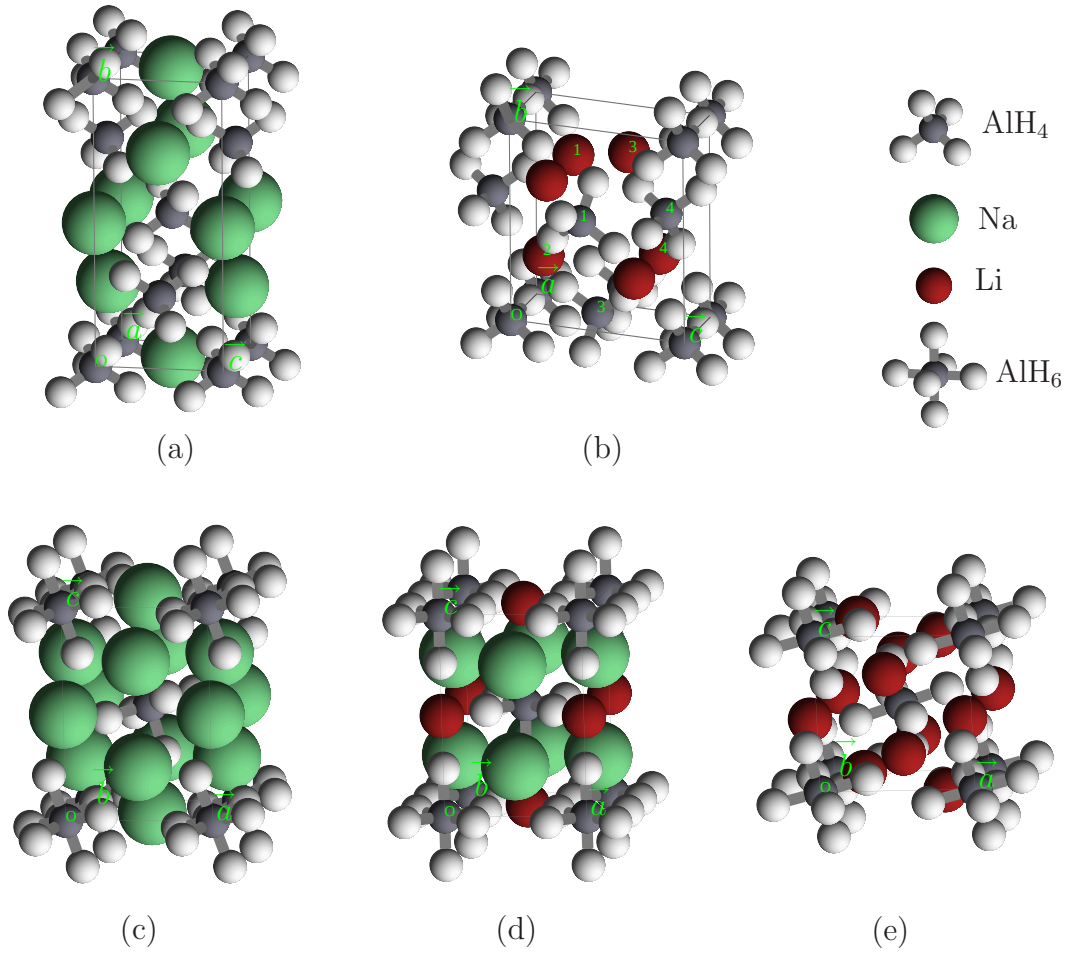

Figure 1: (Color online) Ball-and-stick model of structures of sodium and lithium alanates: (a) $NaAlH_4$ (tetragonal); (b) $LiAlH_4$ (monoclinic); (c) Na_3AlH_6 (monoclinic); (d) Na_2LiAlH_6 (cubic); (e) Li_3AlH_6 (trigonal). The large green spheres stand for Na atoms. The small red spheres stand for Li atoms. The grey sphere at the center of a complex stands for the Al atom, surrounded by 4 or 6 white spheres representing H atoms. Presented are four formula units per unit cell for tetrahydrides (two primitive cells for $NaAlH_4$) and two formula units per unit cell for octahydrides (two primitive cells for Na_2LiAlH_6).

of these complex hydrides are the negatively charged tetrahedral complex AlH_4 or the octahedral complex AlH_6 and the positively charged Na/Li ions. Al and H ions are covalently bonded but of strong ionic nature (with most of valence charge near H); AlH_n complexes and Na/Li cations are ionicly bonded [24]. Conventional cells are shown for $NaAlH_4$ and Na_2LiAlH_6. Unit cells are presented in such a way that the atom-by-atom mapping relation between different structures can be seen. Table 3 lists the calculated lattice parameters for these alkali alanates. The calculated values are in good agreement with available experimental data.

The ground state of $NaAlH_4$ crystalizes in a tetragonal structure (space group $I4_1/a$) with a lattice constant ratio c/a ~2.24. The ground state of $LiAlH_4$ crystalizes in a monoclinic structure (space group $P2_1/c$) with a similar lattice constant a to that of $NaAlH_4$, and lattice constant ratios $b/a \sim c/a$ ~1.62 and β=112.228°. $LiAlH_4$ is predicted to experience a phase transition under a 2.6 GPa pressure, changing from the monoclinic $P2_1/c$ structure to a tetragonal $I4_1/a$ structure with a big volume collapse (~20%) [25]. Our calculation shows that the energy difference of the two phases is only about 60 meV/formula unit. Notice that the point group associated with space group $P2_1/c$ is the subgroup of that associated with $I4_1/a$ with the monoclinic $\vec{b}$ axis corresponding to the tetragonal $\vec{c}$ axis. It is also seen in Table 3 that for the ground state of complex hydrides in the form of $M_x(AlH_4)_y$, the volume per AlH_4 (which shows how closely the complexes are packed together) is about the same. In search of possible Na-Li mixed alanates, it is natural to wonder what happens in the transition process between these two structures mentioned above.

Reasonable initial geometry construction is essential for accelerating the search of possible Na-Li alloyed alanates. A good starting point should be based on all relevant structures and at the same time general enough to lead to potential energy-minima. Previous efforts in this search are either restricted to the $NaAlH_4$ structure [32], or based on a few presumed model structures [33]. Due to the structural connection

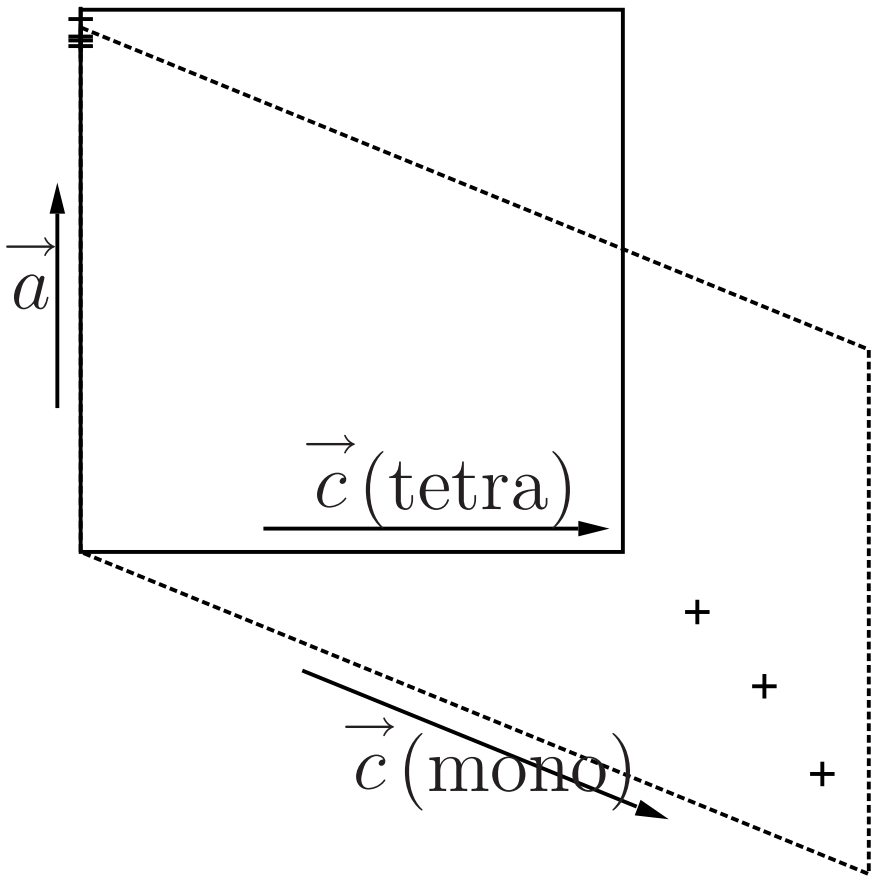

Figure 2: Path for the transition in $Na_{1-x}Li_xAlH_4$ system. The figure shows the change in the unit cell shape in the a-c basal plane as x varies from 0 (tetragonal) to 1 (monoclinic).

between pure sodium and lithium alanates discussed above, we construct the alloyed system $Na_{1-x}Li_xAlH_4$ by assuming a "phase transition" path from tetragonal $NaAlH_4$ to monoclinic $LiAlH_4$. The same volume per AlH_4 complex (as in $NaAlH_4$) is assumed. Figure 2 shows the transition of the unit cell shape as a linear function of lithium composition x. Lattice constants b, c, and angle β differ greatly in pure Na and Li alanates and are therefore made to change with x linearly. Lattice constant a is then determined by the constant-volume constraint. Initial atomic coordinates for Na/Li, Al, and H can also be determined by linear interpolation with x. Alternatively, for each AlH_4 complex, just the position of the Al atom is linearly interpolated; the complex itself is positioned as a whole. In addition, Na and Li atoms can be arranged

on a set of alkali coordinates in different configurations. The starting construction for a certain composition is therefore not unique and can be varied. Initial geometry of the alloy system $Na_{3(1-x)}Li_{3x}Al_6$ is constructed similarly. Unlike the tetrahydrides, Na_3AlH_6, Li_3AlH_6, and Na_2LiAlH_6 have quite different volume per AlH_6. All three lattice constants and three angles are interpolated linearly with x, discarding the constant volume assumption.

3.4 Energy Of Formation And Equilibrium Structures

The process of forming alloyed Na-Li alanates can be expressed as the following reactions:

$$(1 - x)NaAlH_4 + xLiAlH_4 = Na_{1-x}Li_xAlH_4 \tag{74}$$

$$(1 - x)Na_3AlH_6 + xLi_3AlH_6 = Na_{3(1-x)}Li_{3x}AlH_6 \tag{75}$$

The energy of formation E_x^f (with respect to pure sodium and lithium alanates) is defined as

$$E_x^f = E_{tot}^x - [(1 - x)E_{tot}^0 + xE_{tot}^1] \tag{76}$$

where E_{tot}^x is the total energy per formula unit of $Na_{1-x}Li_xAlH_4$ or $Na_{3(1-x)}Li_{3x}Al_6$. Negative energy of formation is necessary for such alloyed systems to exist. Results for the calculated formation energy of these two alloyed systems are shown in Figure 3. Calculation is done at x= 0.25, 0.5, and 0.75 for $Na_{1-x}Li_xAlH_4$; and $\frac{1}{3}$, 0.5, and $\frac{2}{3}$ for $Na_{3(1-x)}Li_{3x}Al_6$. For each x, the atomic positions, cell size, and cell shape are fully relaxed.

In Figure 3 (a), the positive energy of formation indicates that the alloy system $Na_{1-x}Li_xAlH_4$ is not stable, and prefers a phase-separated state of pure $NaAlH_4$ and $LiAlH_4$. The energy difference between the alloyed and phase-separated state is however very small ($<$ 5 kJ/mol), comparable to the room temperature thermal energy (blue dash line in Figure 3 (a)). This means that the meta-stable alloyed system might be stablized at high enough temperature.

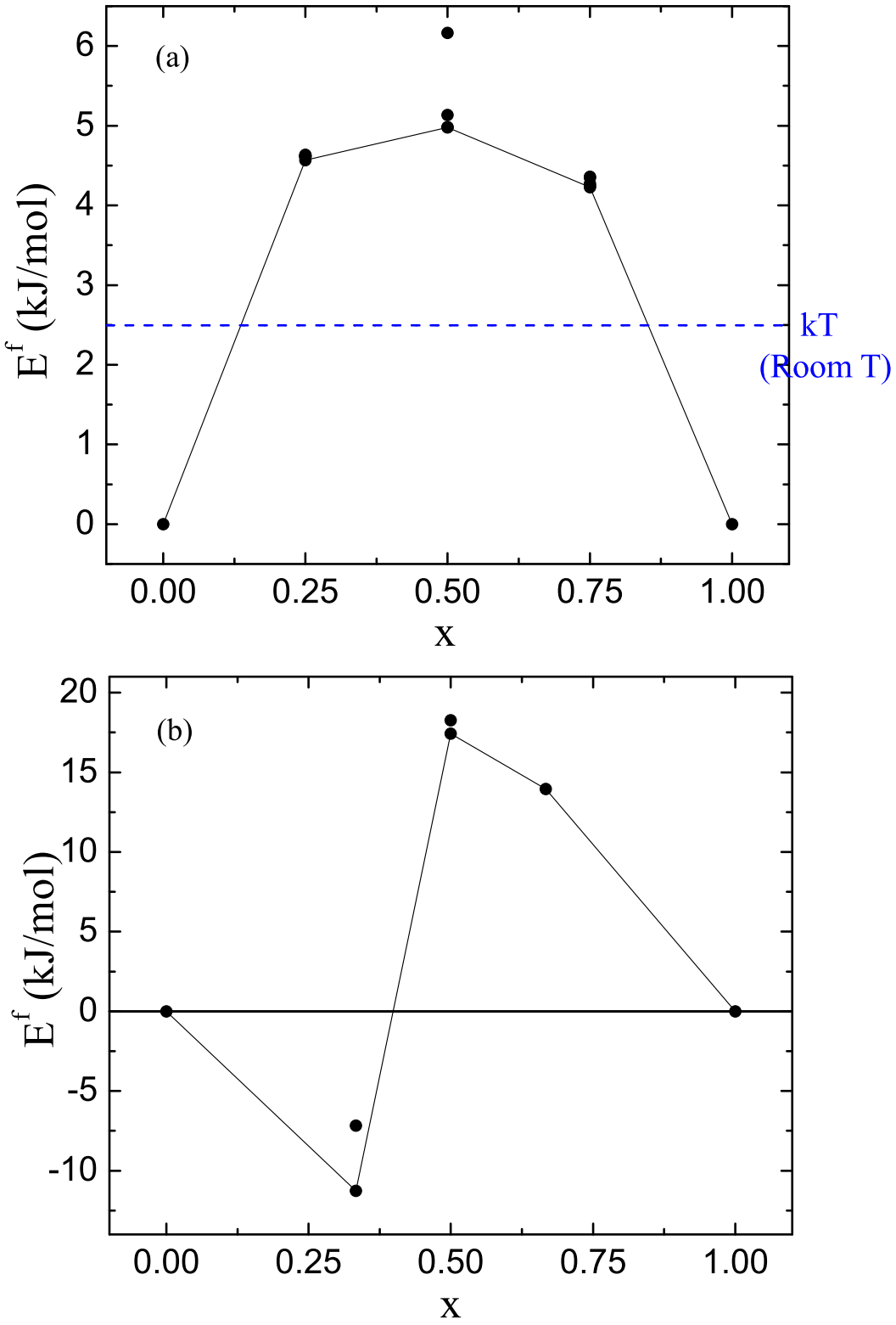

Figure 3: (Color online) Calculated formation energy for (a) $Na_{1-x}Li_xAlH_4$, where blue dash line shows thermal energy level at room temperature; (b) $Na_{3(1-x)}Li_{3x}Al_6$, where for x=$\frac{1}{3}$, calculation is also done at experimental Na_2LiAlH_6 structure (upper point).

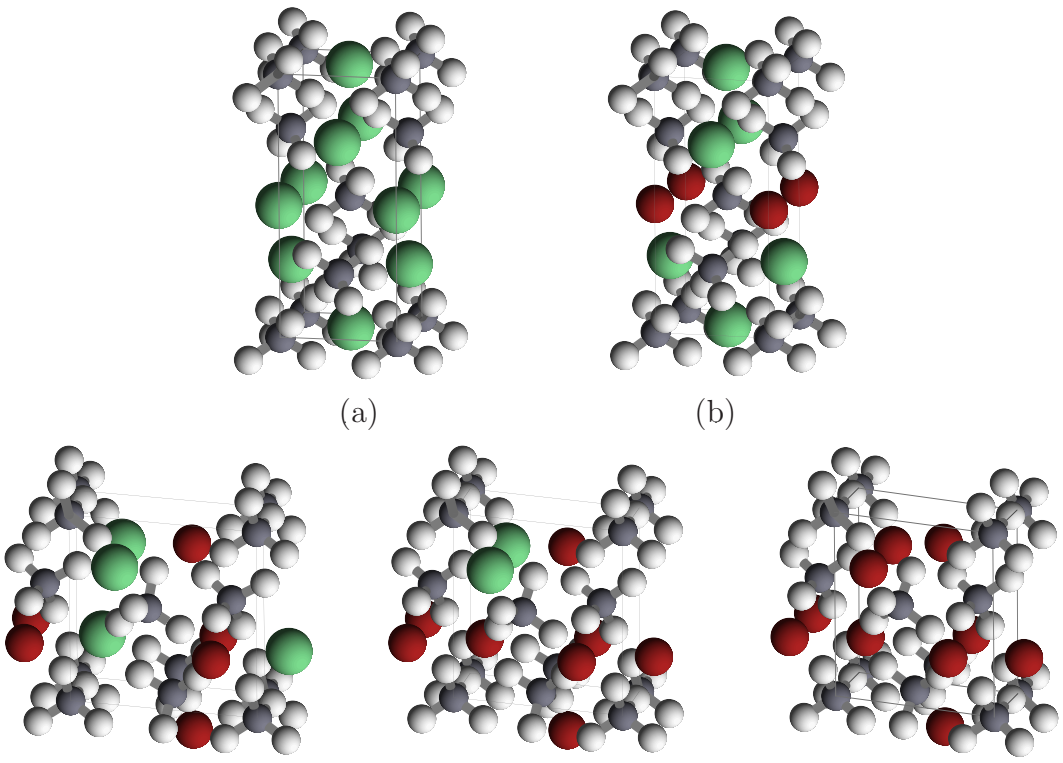

Figure 4: (Color online) Equilibrium structure of $Na_{1-x}Li_xAlH_4$ with x equal to (a) 0.0, (b) 0.25, (c) 0.5, (d) 0.75, and (e) 1.0. For reference, structures of pure Na and Li alanates are also included: (a) $NaAlH_4$ and (e) $LiAlH_4$. A noticeable structural change is found between 0.25 and 0.5 for the tetrahydride.

For the alloy system $Na_{3(1-x)}Li_{3x}Al_6$ (Figure 3 (b)), a stable structure is found at x=$\frac{1}{3}$ (i.e., Na_2LiAlH_6) in agreement with the experimental findings [30]. The calculated formation energy is -11.26 kJ/mol. Formation energy also is calculated with the experimental structure. Relaxation of the linear construction leads to slightly deviated structure from the experimental one, with the number of symmetry lowered from 16 to 1. Total energy is lowered by the amount of 4.08 kJ/mol due to symmetry-breaking in this process. Positive energy of formation is found at the other two lithium compositions.

Figures 4 and 6 show the equilibrium structures of the two alloy systems. For each x, the structure with the lowest formation energy is presented. x=0 and 1 are

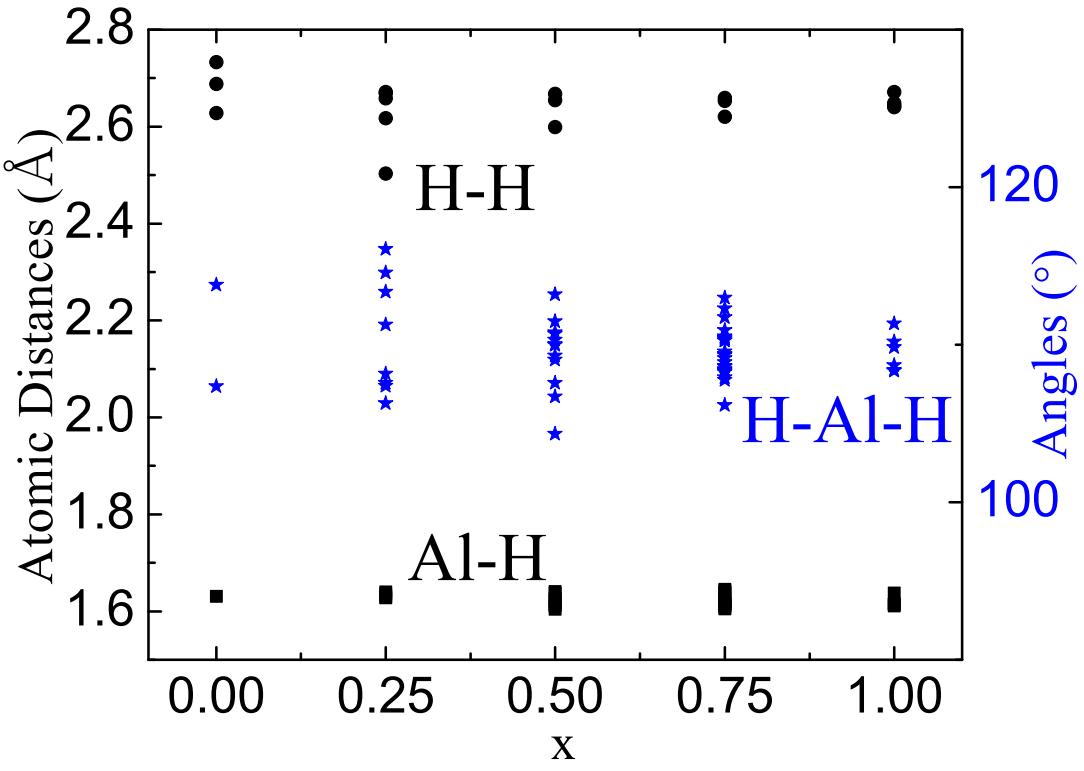

Figure 5: (Color online) Structural parameters of the AlH_4 complex as a function of lithium composition in the equilibrium alloy phases for $Na_{1-x}Li_xAlH_4$.

included as references.

For $Na_{1-x}Li_xAlH_4$, the common feature of the AlH_4 tetrahedral complex is always present, with similar Al-H and H-H bond lengths and H-Al-H bond angles, as shown in Figure 5. Cation substitution has little effect on the internal geometry of AlH_4, and the complexes are packed together with each of them basically intact. For x=0.25, partial substitution of Na by Li does not result in much structural change. Relaxation leads to the same tetragonal symmetry as $NaAlH_4$, as shown in Figure 4 (a) and (b). In fact, symmetry is increased compared with the initial construction.

For $Na_{3(1-x)}Li_{3x}Al_6$, the lowest-energy structure at x=$\frac{1}{3}$ is orthorhombic and is close to the experimental *fcc* structure [30] with similar Al-H bondlengths of 1.75 and 1.76 Å, and a small difference in the H-Al-H angle (less than 0.4°), as shown in Figures 6 (a) and (b). The AlH_6 complexes are slightly tilted and rotated (in

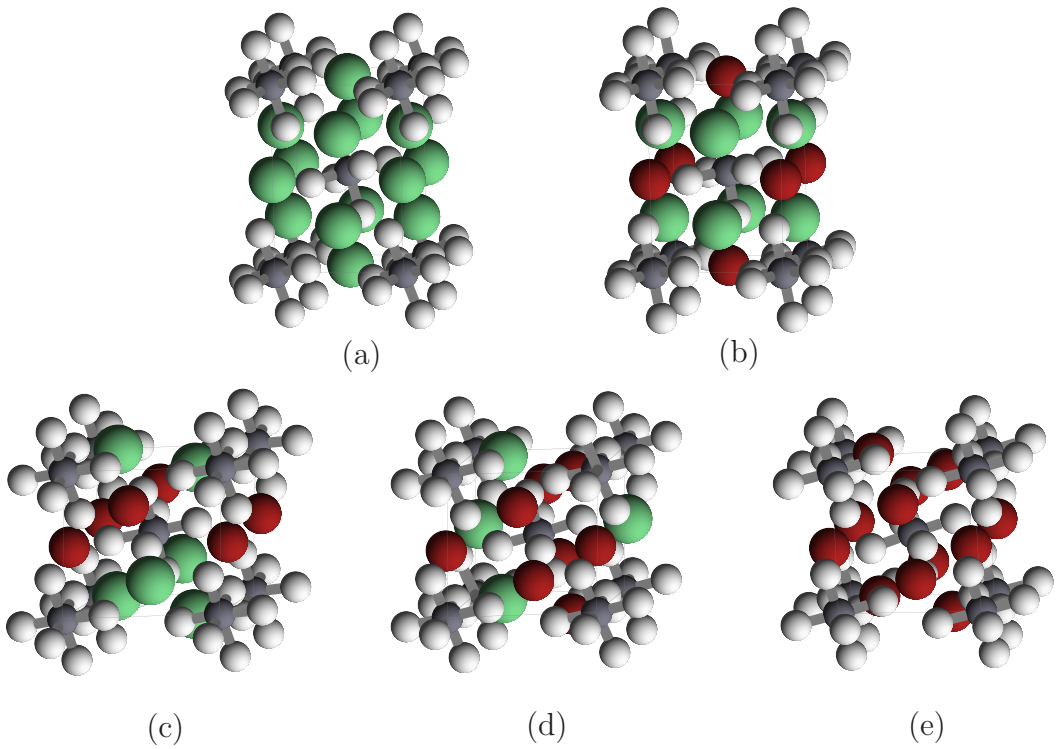

Figure 6: (Color online) Equilibrium structure of $Na_{3(1-x)}Li_{3x}Al_6$ with x equal to (a) 0.0, (b) $\frac{1}{3}$, (c) 0.5, (d) $\frac{2}{3}$, and (e) 1.0. A noticeable structural change is found between $\frac{1}{3}$ and 0.5 for the hexahydride.

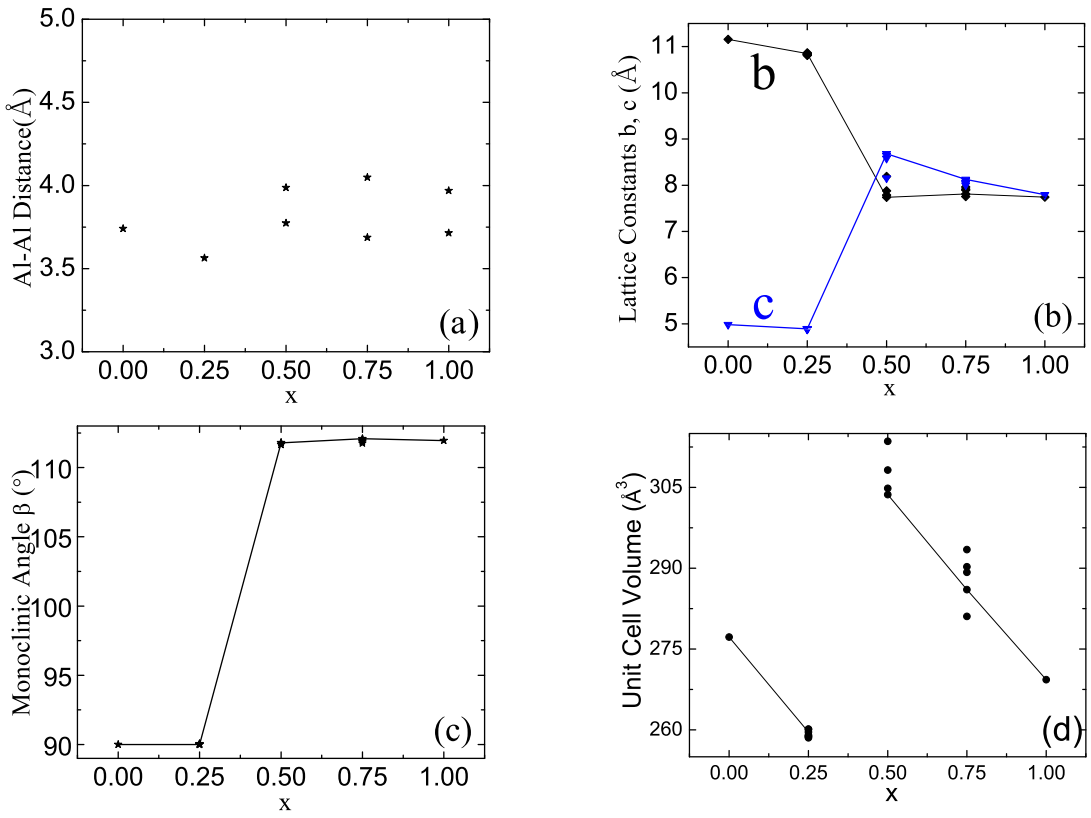

Figure 7: (Color online) Structural parameters of $Na_{1-x}Li_xAlH_4$ as a function of lithium composition x in equilibrium alloy phases: (a) Al-Al distance; (b) lattice constants b and c; (c) monoclinic angle β; and (d) unit cell volume. Data for structures with energies above the lowest energy are also included. Lines are used to connect points corresponding to the lowest energy configurations.

different direction for the corner and body-center complexes) compared with the *fcc* case. Lattice constants are also similar, with a difference of ∼0.01 Å.

In contrast to the initial linear construction, a drastic structural change is seen as x passes 0.5 for both alloy systems. The equilibrium structures are close to sodium alanates for x <0.5 (Figure 4 (a) and (b), and Figure 6 (a) and (b)); and to lithium alanates for $x \geq$0.5 (Figure 4 (c) and (d), and Figure 6 (c) and (d)). To show this more clearly, we plot in Figures 7 and 8 the variations of different structural parameters as the lithium composition of the system changes.

The alloyed system $Na_{1-x}Li_xAlH_4$ undergoes a structural transition at x=0.5. Lattice constants b, c, and angle β are close to those of tetragonal $NaAlH_4$ for x <0.5,

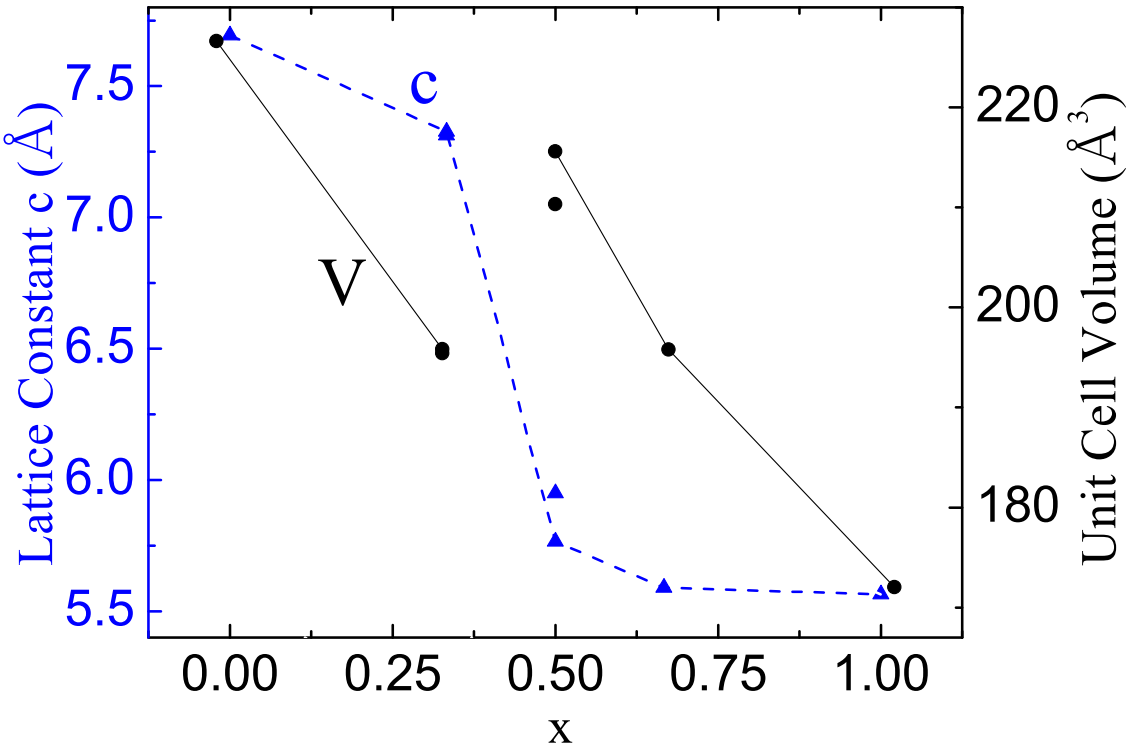

Figure 8: (Color online) Structural parameters of $Na_{3(1-x)}Li_{3x}Al_6$ as a function of lithium composition x in equilibrium alloy phases: lattice constant c and unit cell volume. Data for structures with energies above the lowest energy are included, too. Lines are used to connect points corresponding to the lowest energy configurations.

and to those of monoclinic $LiAlH_4$ for $x \geq 0.5$, as shown in Figures 7 (b) and (c). The bond length for nearest-neighbor Al atoms bifurcates at 0.5 (Figure 7 (a)) again showing the structural transition between 0.25 and 0.5. Within each structure, the volume per AlH_4 complex drops as x increases (Figure 7 (d)), which can be explained by the smaller size of lithium ion with respect to the sodium ion. The slightly positive energy of formation therefore may be due to packing volume deviating from the experimental value (Table 3, data in red) considering that both sodium and lithium have the same valence. If the constant-volume condition shall hold for $Na_{1-x}Li_xAlH_4$, it will probably be in a structure different from either $NaAlH_4$ or $LiAlH_4$.

For the alloy system of $Na_{3(1-x)}Li_{3x}Al_6$, as x goes from 0 to 1, the largest change is in the lattice constant c and volume per AlH_6 complex, as shown in Figure 8. Like

in the previous case, a structure transition is noted between x=$\frac{1}{3}$ and x=0.5. The structure of the alloy is close to Na_3AlH_6 for x <0.5 and to Li_3AlH_6 for x ≥0.5. Similarly, within each structure, volume decreases as lithium composition increases (again as a result of a smaller ion size of lithium than sodium).

3.5 Summary

Based on the structures of pure sodium and lithium analates, we construct the Na-Li alloyed alanates $Na_{1-x}Li_xAlH_4$ and $Na_{3(1-x)}Li_{3x}AlH_6$ through structural interpolation. We also examine their energetics and structural properties by means of first principles calculations.

A small positive energy of formation (<5 kJ/mol) is found for $Na_{1-x}Li_xAlH_4$ with x=0.25, 0.5, and 0.75. In other words, no stable phases are found. The equilibrium structure experiences a transition from the tetragonal $NaAlH_4$ structure to the monoclinic $LiAlH_4$ structure between x=0.25 and 0.5. Within each structure volume decreases with increasing x, which can be explained by the smaller ion size of Li than Na. Besides these two no other structure is reached, which shall be necessary if the condition of a constant-volume per AlH_4 is to be satisfied considering that Na and Li have the same valence.

Negative energy of formation is found for Na_2LiAlH_6 consistent with the experimental finding. The calculated structure is slightly deviated from the experimental one, with lowered symmetry and slightly lowered energy. No stable structure is found for $Na_{3(1-x)}Li_{3x}AlH_6$ at x=0.5 and $\frac{2}{3}$. The equilibrium structure experiences a transition from the monoclinic Na_3AlH_6 to the trigonal Li_3AlH_6 structure between x=$\frac{1}{3}$ and 0.5. Within each structure, volume decreases with increasing x, which again can be explained by the smaller ion size of Li than Na.

CHAPTER IV

FIRST-PRINCIPLES INVESTIGATION OF THE LI-MG-N-H SYSTEM

4.1 Introduction

A few years ago, Chen *et al.* [34] reported a hydrogen storage system based on the interaction of H_2 with lithium imide, Li_2NH, forming lithium amide, $LiNH_2$, and lithium hydride. About 6.5% of H_2 by weight can be reversibly stored in this Li-N-H system, with a plateau pressure of 1 *bar* at a relatively high temperature of 285°C. In order to use this system for mobile hydrogen storage, H_2 needs to be absorbed/desorbed at higher pressure and a lower temperature [34, 35, 36, 37, 38, 39, 48]. One possible way to achieve this is to reduce the reaction enthalpy by means of cation substitution with elements of greater electronegativity (such as Ca, Al, and B) than Li [38, 39, 40, 41, 42, 43, 44, 45, 46, 47]. Luo *et al.* reported such a new Li-Mg-N-H system, by substituting lithium hydride with magnesium hydride [38, 48, 49, 50]:

$$2LiNH_2 + MgH_2 \rightarrow Mg(NH_2)_2 + 2LiH \quad (77)$$

$$Mg(NH_2)_2 + 2LiH \leftrightarrow Li_2Mg(NH)_2 + 2H_2 \quad (78)$$

The starting material, $2LiNH_2$+MgH_2, undergoes reaction (77) and changes into magnesium amide and lithium hydride at 220°C and under 100 *bar* of H_2 [50]. The reversible reaction follows Equation (78) with the $Mg(NH_2)_2$:LiH molar ratio of 1:2. By introducing Mg into the original Li-N-H system, the plateau pressure is raised to ∼30 *bar* at a lower temperature of 200°C, while maintaining an acceptable hydrogen capacity of ∼5% by weight. Cycling tests of this system also show good reversibility. The Li-Mg-N-H systems with the Mg:Li molar ratios of 3:8 and 1:4 also are reported

[45, 46, 47, 51, 52, 53] where altering the molar composition modifies the hydrogen capacity, thermodynamics, kinetics, and even reaction path of the hydrogen storage system [41]. In addition, Alapati *et al.* proposed a reaction with a Mg:Li molar ratio of 1:1 [54] where a product of the mixed nitride LiMgN is suggested.

As shown above, the Li-Mg-N-H system, as a promising hydrogen storage material, has much potential of further optimization. In order to understand the phase stability and energetics of the above reactions, it is necessary to first understand all the ground state crystal structures involved. The crystal structure of the mixed imide $Li_2Mg(NH)_2$, which appears for the Mg:Li ratio of 1:2 as in Equation (78), is not determined until recently. Rijssenbeek *et al.* [55] investigated the component structures in the hydrogen desorption/absorption process in the Li-Mg-N-H system with in-situ X-ray diffraction (XRD). Their study shows that $Li_2Mg(NH)_2$ undergoes progressive disordering of the cations and the cation vacancies as temperature is increased, resulting in two structural transitions at elevated temperatures. The corresponding three high temperature structural variants of $Li_2Mg(NH)_2$ are determined, via a combination of X-ray and neutron powder diffraction, to be orthorhombic (α) phase, primitive cubic (β) phase, and face-centered cubic (γ) phase, as shown in Figure 9. In all three phases, nitrogen atoms form an *fcc* lattice (although slightly distorted), similar to the arrangement in lithium imide/amide and magnesium amide [56]. The cations are located at the tetrahedral interstitial sites of this *fcc* lattice. Not all of the tetrahedral interstitial sites are occupied. In the room temperature α phase, 25% of the tetrahedral sites are ordered vacancies, and lithium and magnesium occupy the remaining 75% of the tetrahedral sites in a disordered fasion (Figure 9(b)).

As temperature is raised above 350°C, the α phase converts into the β phase (Figure 9 (c)), where some of the tetrahedral sites (3c) are disorderly occupied by Li and Mg, and some others (3d) are partially occupied by Li, leading to disordered arrangement of both cation and cation-vacancy. The β phase disorder is still partial

since a fraction of the tetrahedral sites are orderly occupied by either Li or vacancy. When temperature is raised above 500°C, the β phase converts into the γ phase, where all the tetrahedral sites are disorderly occupied by Li, Mg, and vacancies (Figure 9 (d)). In β-$Li_2Mg(NH)_2$, the experimental Li:Mg:vacancy occupancy ratio for Wyckoff positions 3d and 3c are 59:8:33 and 41:59:0, respectively. In γ-$Li_2Mg(NH)_2$, this ratio for Wyckoff position 8c is 11:4:5.

In this work, we concentrate on the ground-state structure of this system. Starting from the experimental α-disordered structure, we search systematically for the low-energy configurations of $Li_2Mg(NH)_2$ via *ab initio* total energy calculations. A series of such configurations is found. By observing features commonly present in these low energy configurations, specific local orderings are found in the cation-vacancy arrangement, and their relation with the experimental disordered models is discussed. Possible low-energy ordered structures are proposed for $Li_2Mg(NH)_2$. In addition, the reaction energetics for the Li-Mg-N-H systems are calculated, and the phase stability is discussed.

4.2 Computational Details

Here we outline the methods and calculational details involved in this work. The main method we employ is first-principles calculation within the density functional theory (DFT) [5]. The calculation is based on total energy and force/stress calculations in momentum space with plane-wave basis and is done with the Vienna ab-initio simulation package (VASP) [20] using the projector augmented wave (PAW) method [17], with the generalized gradient approximation (GGA) [18] for the exchange-correlation energy functional. The kinetic energy cutoff of the plane-wave basis is chosen to be 850 eV, and a k-grid interval of ~ 0.3 Å^{-1} is used for reciprocal space sampling, so that the total energy convergence is achieved under these conditions. For structural relaxations, all forces and stresses are relaxed simultaneously. The force is considered

to be minimized if the magnitude on any atom is smaller than 0.01 eV/Å. In order to compare directly our low-energy structures with the experimental data, we also calculated total energies for various configurations with the unit cell parameters fixed at the room-temperature experimental values (Table 4). For the energetics study, the reaction enthalpy is approximated as the difference between the total energies of the products and the reactants, omitting the zero point energy and the PV term.

4.3 Results and Discussions

4.3.1 Low-energy structures of $Li_2Mg(NH)_2$

At room temperature α-$Li_2Mg(NH)_2$ is reported to have an orthorhombic crystal structure with space group *Iba2*. As shown in Figure 9 (b), the nitrogen atoms approximately form an *fcc* lattice, where 3/4 of the tetrahedral interstitial sites can be labeled by two kinds of crystallographically distinct cation sites with Wyckoff notations of 8c and 4b, respectively, while the other 1/4 are cation vacancies. The cation vacancies are ordered, and form linear chains along lattice vector $\vec{c}$, so that each N-H unit can point toward a midpoint between two adjacent cation vacancy sites in an orderly manner. The 8c and 4b sites are randomly occupied by both kinds of cations, with an experimentally reported Li:Mg occupancy of 75.2%:24.8% on 8c and 62.6%:37.4% on 4b sites, respectively, as determined by XRD data [55].

We have searched systematically the possible low-temperature Li-Mg arrangements in Wyckoff positions of 8c and 4b for space group *Iba2*, with the overall constraint of Li:Mg equal to 2:1. Table 4 lists the calculated total energies and lattice parameters of various configurations after full minimization of forces and stresses. Low-energy configurations are labeled by A, B, C, etc. For comparison, the total energy with lattice parameters fixed at experimental values is also calculated and listed. A few selected low-energy configurations are shown in Figure 10.

For configurations C, E, F, G, and GG, an occupancy of Li:Mg equal to 3:1 on 8c

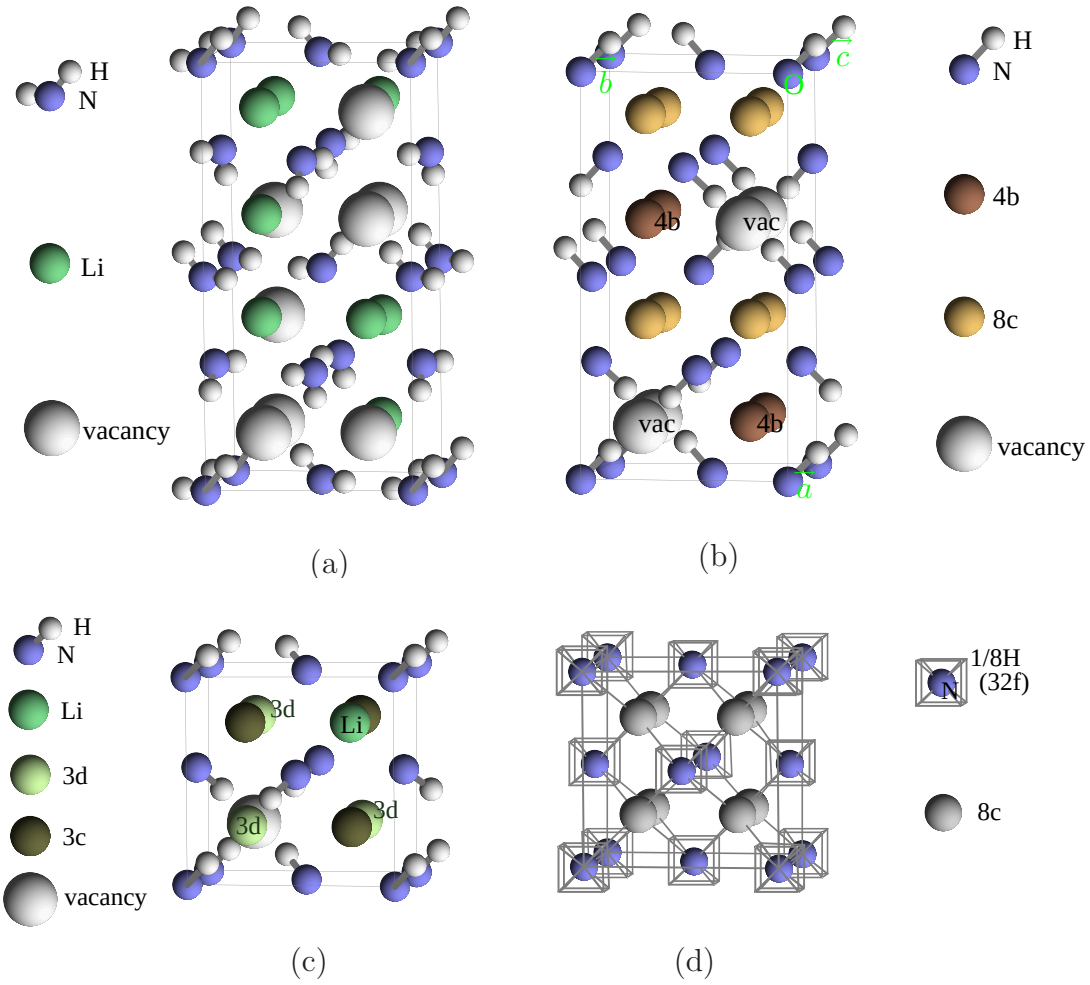

Figure 9: (Color online) Ball-and-stick models for (a) $LiNH_2$, (b) α-$Li_2Mg(NH)_2$, (c) β-$Li_2Mg(NH)_2$, and (d) γ-$Li_2Mg(NH)_2$. The origin is set at a N atom. The large light spheres in (a)-(c) represent (cation-)vacancies. (b)-(d) show the specific cation (and cation-vacancy) disordered features of the Li-Mg mixed imide [55]. Li amide is also shown in (a) to demonstrate the structural features of *fcc* $(NH_2)^-/(NH)^{2-}$ network common to these imides/amides.

Table 4: List of calculated total energies (per formula unit) E_{tot} and lattice parameters for various $Li_2Mg(NH)_2$ ordered configurations. Data in parentheses are calculated by fixing the lattice parameters at the experimental values. Configurations of low energies are labeled A, B, C, etc. Also listed are the calculated volume (per N atom) $\tilde{v}$ and the number of symmetry operations Z. Experimental data are listed for comparison.

Configu-	E_{tot}	Unit cell parameters						$\tilde{v}$	Z
-rations	(eV/f.u.)	a (Å)	b (Å)	c (Å)	$\alpha(^\circ)$	$\beta(^\circ)$	$\gamma(^\circ)$	(Å^3)	
A	-33.09	9.60	5.14	5.36	90.	89.97	90.	33.04	2
B	-33.17(-33.12)	10.02	4.80	5.33	90.	90.	90.	32.03	4
C	-33.14(-33.14)	9.76	4.98	5.22	90.	90.	89.98	31.73	2
D	-33.15(-33.14)	9.73	5.08	5.25	90.46	89.97	89.97	32.40	1
E	-33.16(-33.16)	9.77	4.99	5.22	90.	89.86	90.	31.82	2
H′	-33.18(-33.17)	9.68	5.10	5.21	90.	90.	90.11	32.27	2
F	-33.19(-33.18)	9.84	4.99	5.25	90.	90.	89.98	32.22	2
G	-33.20(-33.20)	9.83	5.00	5.25	89.43	90.01	89.96	32.26	1
H	-33.22(-33.21)	9.70	5.10	5.21	90.	90.	90.	32.26	4
supercell calculations in direction $\vec{b}$:									
DD(4b)	-33.15(-33.14)	9.78	5.05	5.25	90.	89.98	90.	32.39	2
GH(4b)	-33.20(-33.20)	9.76	5.05	5.23	90.	89.97	90.	32.22	2
GG(2b)	-33.23(-33.22)	9.84	4.97	5.24	90.	89.97	90.	32.04	2
Experiment [55]:		9.7880	4.9931	5.2023	90.	90.	90.	31.78	4

(and 1:1 on 4b) sites are assumed, in accordance with the experimental conclusion. In this case, the calculated lattice parameters differ little from experimental values, and the difference of the total energy is also very small between the fully relaxed structure and that with lattice parameters fixed at the experiment values.

It is noticed that the inconsistency in experimental 8c/4b cation occupancies renders a total Li:Mg ratio of 2.45:1, in contradiction with the overall 2:1 ratio [55]. With the possible uncertainties of the experimental data in mind, we also consider 8c-site occupancies beyond 3:1. For configuration A, B, D, DD, H, and GH, the Li:Mg occupancy ratios at the 8c/4b sites are 1:1/1:0, 1:0/0:1, 5:3/3:1, 5:3/3:1, 1:1/1:0, and 5:3/3:1, respectively. Because of the deviation from the experimental ratios, the calculated lattice parameters slightly differ from experiment values.

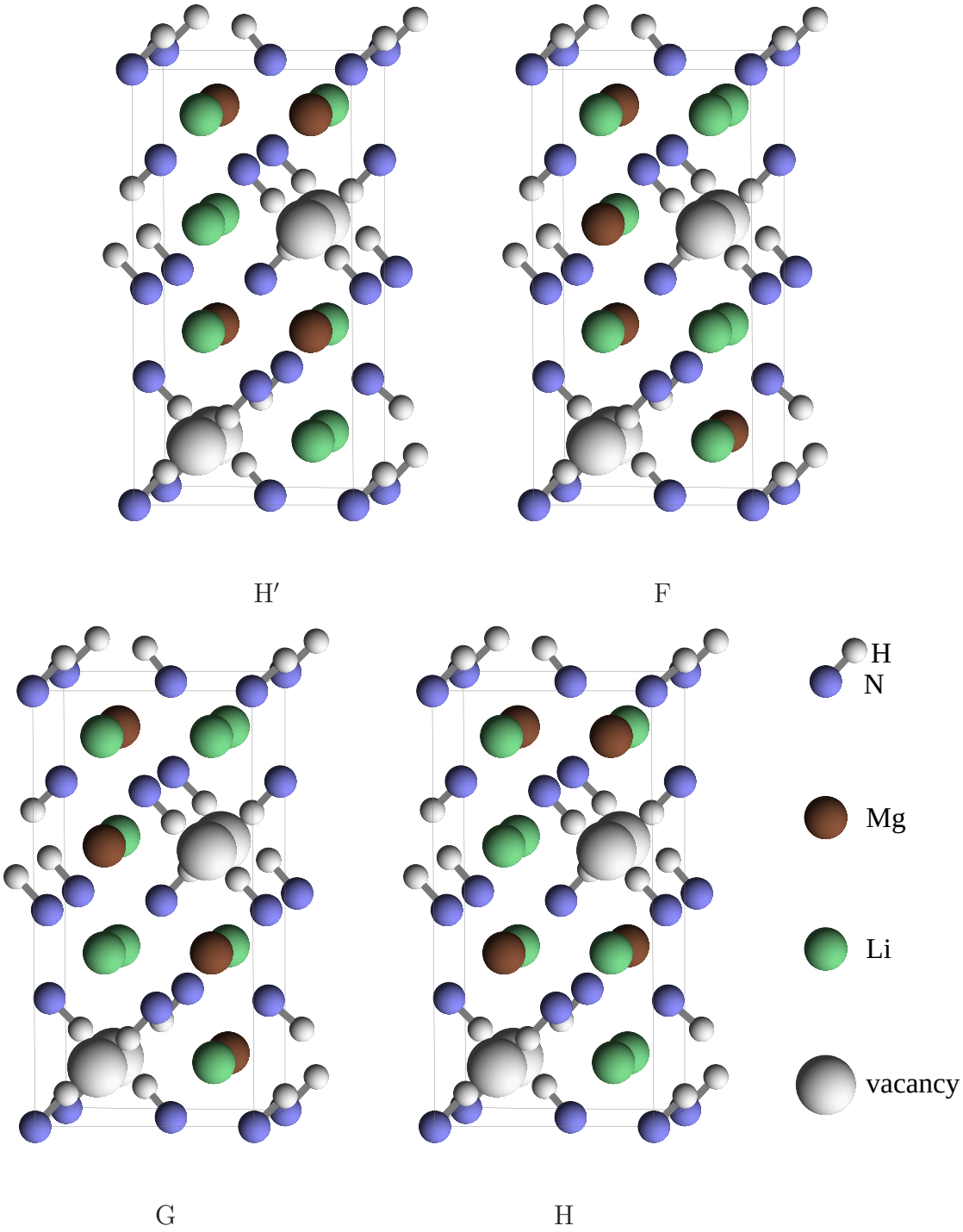

Figure 10: (Color online) Some of the low-energy configurations in Table 4.

In all cases, the change in cell volume due to the difference in the Li/Mg arrangement is rather small (<4%), which is expected because of the similar ionic radii of Li and Mg [59]. The change in angles is also small ($\leq 0.5^\circ$), and does not affect much the total energy (configurations D and G).

Our calculation shows that for configurations with different cation arrangements on the 8c and 4b sites, the differences in the total energy are rather small, generally in the order of 10 meV per formula unit $Li_2Mg(NH)_2$. (such as C, D, E, I, II, III, and IV). Multi-configurations of cation arrangements with small energy differences indeed suggest possible Li/Mg disordered arrangements in the crystal structure of α-$Li_2Mg(NH)_2$, as reported in experiment.

4.3.2 Local orderings in $Li_2Mg(NH)_2$

By examining the low-energy configurations, we find that certain local Li-Mg-vacancy arrangements are preferable. Table 5 lists the fractional occurrence of various local orderings for each configuration listed in Table 4. The local orderings are illustrated in Figures 11 and 12, where one N-H unit is surrounded by eight adjacent tetrahedral sites associated with an *fcc* lattice. In Figure 12, the neighboring "cube" encasing an octahedral interstitial site is also shown. From Table 5, it is obvious that the total energy and local orderings exhibit correlations.

The energetically preferable local orderings can be described as the following: two Mg atoms order in a face-diagonal arrangement on the NH-enclosing cube, where two cation-vacancy sites line up on one side, with the N-H unit pointing in between. The vacancy chain is either (a) off (and parallel to) the plane containing Mg atoms, with the N-H unit pointing away from the Mg-containing plane, as shown in Figure 11 (a); or (b) perpendicular to the Mg-containing plane, with the N-H unit being almost parallel to (yet still pointing slightly away from) the Mg-containing plane, as shown in Figure 11 (b).

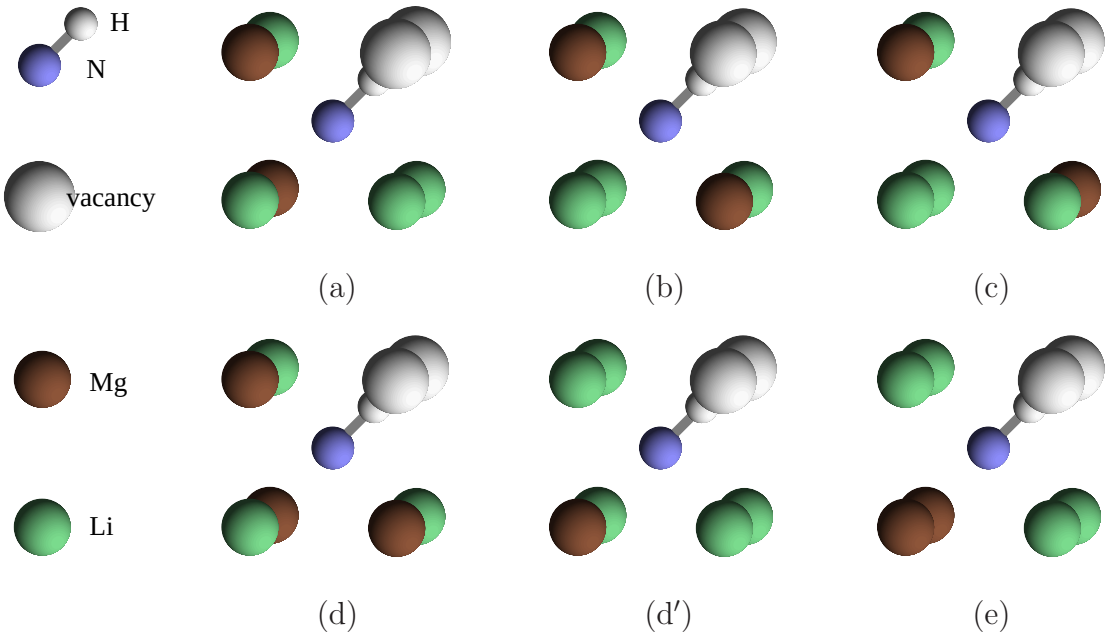

Figure 11: (Color online) Local orderings for the Li-Mg-vacancy arrangement, where a N-H unit is surrounded by eight adjacent tetrahedral sites associated with an *fcc* lattice. Two of the eight surrounding tetrahedral sites are (cation-)vacancy sites, which form a linear chain. The N-H unit points toward a midpoint in between. The other six sites are occupied by either Li or Mg. (a) Two Mg atoms in a face-diagonal arrangement, with the hydrogen pointing away from the plane containing Mg atoms; (b) Same as (a), but with the Mg atoms on a different plane; (c) Two Mg atoms in a body-diagonal arrangement; (d) Three Mg atoms surrounding one N-H unit; (d′) One Mg atom around one N-H unit; and (e) Two Mg atoms in a neighboring arrangement. Configurations (c)-(e) are not energetically preferred.

The other local orderings in Figure 11 are not as favorable as the two mentioned above. For (d) and (d′), the distribution of Mg atoms on the cube is uneven, with either one or three Mg atoms per cube, rather than the average number of two. For (e), the Mg-Mg distance is too small when two Mg atoms order on the same side of the cube. For (c), since the N-H unit is already at the center of the body-diagonal plane, there is not much degree of freedom in the arrangement of the hydrogen for it to avoid Mg atoms as in (b). When being "wedged" into a specific configuration, these local orderings in Figure 11 can present themselves in each possible lattice direction, and have basically similar effect in terms of the total energy.

In addition, local orderings at a larger scale can also make a difference in the total energy of a configuration. Within two adjacent cubes (where one of them encases one N-H unit and the other one does not), the preferable local ordering (aa) can be described as (Figure 12): the vacancy chain is in the common face of the cubes, and the four Mg atoms follow two different face-diagonals on the two faces above and below, respectively. The N-H unit (sitting at the center of one of the cubes) points towards the vacancy chain as usual.

As can be seen in Table 5, correlations can be found between the occurrence of local orderings and the total energy. For example, both configurations C and E have 50% face-diagonal (a) and 50% body-diagonal (c) Mg orderings, presenting the same local ordering within the scale of one NH-encasing cube. Along lattice vector $\vec{a}$, configuration C exhibits a pattern of (a)-(a)-(c)-(c), whereas configuration E exhibits a pattern of (a)-(c)-(a)-(c) resulting in a more balanced Mg distribution among lattice layers, and (therefore) a lower total energy.

It is also noticed that, although both have 100% face-diagonal (a) Mg ordering, configuration H has relatively a lower energy than H′. Within the range of two adjacent cubes, Mg atoms order along the same face-diagonal direction on the opposite faces (parallel to each other) in H′; while in H, they order along different face-diagonal

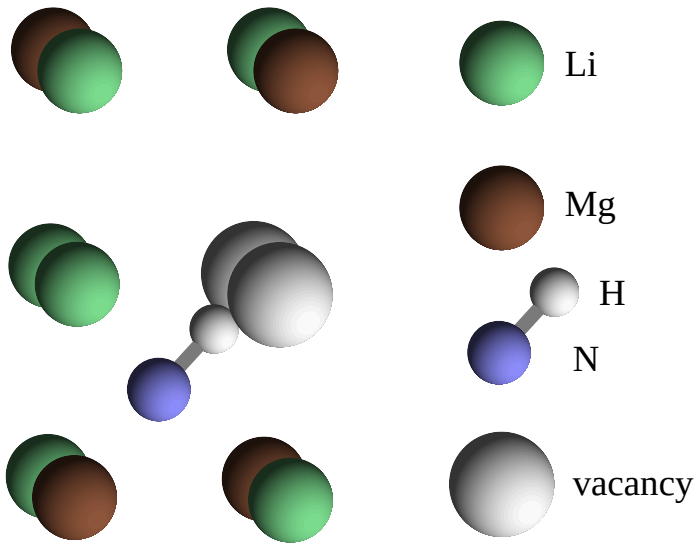

(aa)

Figure 12: (Color online) Local ordering (aa), where the lower cube encases one N-H unit, but the upper one does not. Mg atoms follow different face-diagonal directions on the two faces above and below the common face of the two cubes, and the N-H unit points toward the vacancy chain in the common face, and away from the Mg-containing faces. When placed into the lattice, this local ordering can be along either direction of lattice vector $\vec{a}$ or $\vec{b}$.

directions (perpendicular to each other) on the opposite faces. This leads to higher symmetry and (therefore) a lower total energy in H than in H′, as shown in Figure 10, Table 4, and Table 5.

The same stacking variation can be applied to find other low-energy configurations with such similar orderings. Notice that for each configuration there are equivalent ways (in terms of energy) to define the unit cell. By putting two such equivalents side by side, we get supercell configurations with a larger-scale ordering of Mg atoms along alternating face-diagonal directions (Figure 12). Supercell configuration GG thus constructed has doubled lattice constant along $\vec{b}$, a higher symmetry, and a lower total energy compared with the original single-cell configuration G. It has in fact the lowest energy in Table 4. Note that in GG, the alternation is along $\vec{b}$, while

Table 5: Fractional occurrence of various local orderings for configurations listed in Table 4. Configurations are arranged from left to right with a descending total energy. Local orderings, as shown in Figures 11 and 12, are listed from top to bottom beginning with the most preferable ones. All local orderings are within one cube (Figure 11) except for (aa), which involves two adjacent cubes (Figure 12).

Mg local ordering	fraction in each configuration:												
	A	B	C	DD	D	E	H′	F	G	GH	H	GG
(aa)										$\frac{1}{4}$	1	$\frac{1}{2}$
(a)			$\frac{1}{2}$	$\frac{1}{4}$	$\frac{1}{2}$	$\frac{1}{2}$	1	$\frac{1}{2}$	$\frac{1}{2}$	$\frac{1}{2}$	1	$\frac{1}{2}$
(b)								$\frac{1}{2}$	$\frac{1}{2}$	$\frac{1}{8}$		$\frac{1}{4}$
(c)			$\frac{1}{2}$			$\frac{1}{2}$				$\frac{1}{8}$		$\frac{1}{4}$
(d)				$\frac{3}{4}$	$\frac{1}{2}$					$\frac{1}{4}$		
(e)	1	1										

in H it is along $\vec{a}$. Since vacancies (therefore N-H units) order differently along $\vec{a}$ and $\vec{b}$, this shows that the local ordering (aa), when placed into the lattice along different directions ($\vec{a}$ or $\vec{b}$), differs somehow in terms of lattice symmetry and total energy. In H, this leads to cation occupancies rather different from experimental values, and local ordering (aa) alone does not guarantee lower energy of H than GG. In supercell configuration GH, energy does not drop since unfavorable local orderings also occur.

The concept of local orderings can explain what happens in higher-temperature phases of Li2Mg(NH)$_2$. The structure of β-Li2Mg(NH)$_2$ is similar to that of the α phase, except that now the cation-vacancy chains are no longer fixed to be along $\vec{c}$ but can orient along any of the three lattice-vector directions (Wyckoff position 3d) with equal probability. As shown in Figure 9 (c), the Mg atoms still occupy face-diagonal (3c) sites, and the N-H units point toward the definite vacancy sites and away from the Mg-containing planes, presenting similar local orderings as in α phase. Notice that the face-diagonal arrangement of Mg atoms on the cube formed by tetrahedral

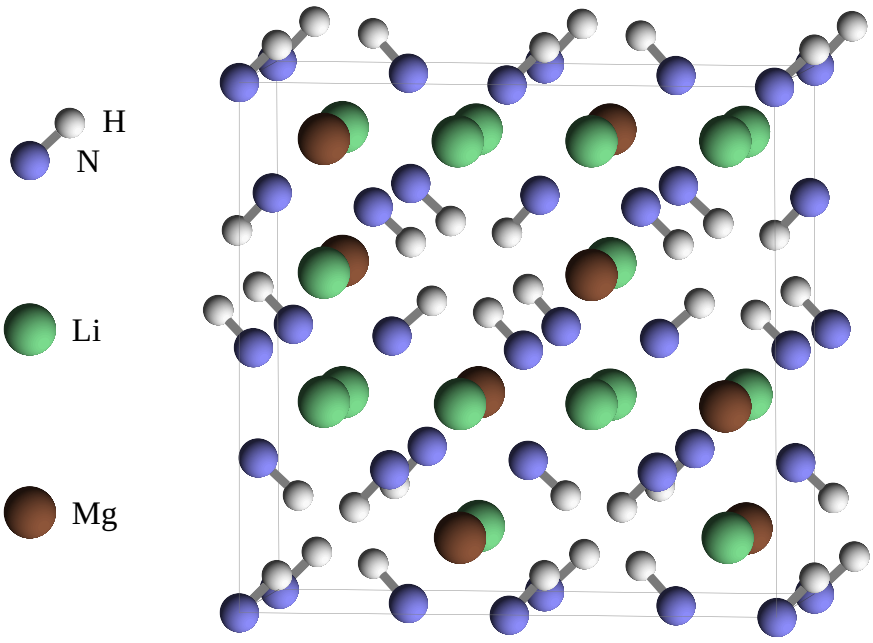

Figure 13: (Color online) A low energy crystal structure (configuration GG in Table 4) proposed for $Li_2Mg(NH)_2$ at lower temperature.

interstitial sites is also found in the structure of $Mg(NH_2)_2$. As temperature is further raised, the β phase transforms into an even more disordered γ phase (Figure 9 (d)), where all tetrahedral interstitial sites are occupied evenly by Li, Mg, and vacancies with a ratio of about 2:1:1.

At lower temperature, the α phase is expected to undergo disorder-order transition, and transform into a low-temperature ordered phase. Based on our calculation of various Li-Mg configurations on the 8c and 4b sites, an ordered crystal structure at lower temperature is proposed, as shown in Figure 13. It is composed of the energetically preferable local orderings and has the lowest total energy of configurations considered so far.

The enthalpy of reaction (calculated as the difference in total energy between products and reactants at 0 K temperature) is listed in Table 6. The zero point energy is not included, which is expected not to change the relative feature in these energies. Our calculation shows that the starting material of $LiNH_2$ + MgH_2 does

Table 6: Calculated enthalpy of reaction (in unit of KJ/mol-H_2) for the Li-Mg-N-H system. Data in parentheses are from experiments.

	Reaction			Enthalpy ΔH (KJ/mol H_2)
(1)	$2LiNH_2 + MgH_2$	$\rightarrow$	$Mg(NH_2)_2 + 2LiH$	-39.62
(2)	$Mg(NH_2)_2 + 2LiH$	$\leftrightarrow$	$Li_2Mg(NH)_2 + 2H_2$	60.89(41.6 [57])
(1)+(2)	$2LiNH_2 + MgH_2$	$\rightarrow$	$Li_2Mg(NH)_2 + 2H_2$	21.67(34 [48])

undergo reaction (77) and transforms into $Mg(NH_2)_2 + 2LiH$ in the first place, and the following cycle reaction proceeds as (78), in agreement with the experimental observations [48, 51].

4.4 Summary

Recently the Li-Mg-N-H system has attracted much attention as a promising solid-state hydrogen storage material [48]. It has the advantage of moderate reaction conditions in addition to the high capacity and reversibility compared with the Li-N-H system. The crystal structure of the mixed imide $Li_2Mg(NH)_2$ involved in this system is not known until quite recently. At room temperature and above, it is reported to have progressive disorder of the cations and vacancies, where the exact arrangement of Li and Mg atoms is not known. Various Li-Mg-N-H systems with different ratios of starting materials (and different products) also raise questions about the phase stability, thermodynamics, and reaction path of this system.

In this chapter, we investigate the crystal structure of $Li_2Mg(NH)_2$ using first-principles total-energy calculations within the density functional theory. The possible cation arrangement in α-$Li_2Mg(NH)_2$ is studied systematically. A series of low-energy ordered configurations are found with similar total energies, indicating possible cation-disordered arrangements, in agreement with the experimental finding. However, energetically preferable local orderings are found, where Mg atoms prefer face-diagonal arrangements on the "cubes" formed by tetrahedral interstitial sites of

an *fcc* lattice, and arrange themselves in alternating face-diagonal directions on opposite faces of two adjacent cubes. Based on our calculation, an ordered structure at lower temperature is proposed for $Li_2Mg(NH)_2$. In addition, reaction energetics is calculated, which confirms the phase stability observed in experiment [41, 48, 51].

CHAPTER V

FIRST-PRINCIPLES INVESTIGATION OF THE LA-MG-PD-H SYSTEM

5.1 Introduction

Recently Yvon *et al.* [61, 60] reported on a new nickel based ternary metal-hydrogen system $LaMg_2Ni$-H in which hydrogenation induces a metal-nonmetal transition:

$$2LaMg_2Ni + 7H_2 \rightarrow 2LaMg_2NiH_7 \tag{79}$$

The intermetallic $LaMg_2Ni$ (orthorhombic, space group Cmcm) absorbs hydrogen around ambient conditions (<8 *bar*, 150∼200°C) to form nonmetallic hydride $LaMg_2NiH_7$. This hydride crystalizes in monoclinic symmetry (space group $P2_1/c$) and has a nearly unchanged metal host structure with atom shifts <0.7 Å. This is in contrast to the usual case of simple systems based on rare earths or magnesium where hydrogenation induced a metal-nonmetal transition accompanied by a major structural rearrangement of the metal host. The metal-nonmetal transition is induced by charge transfer of conduction electrons into tetrahedral $[NiH_4]^{4-}$ complexes with a closed-shell electron configuration. The other hydrogen atoms not associated with the complex remain to be simple saline-like hydride anions surrounded by magnesium and lanthanum atoms (as electron donors). The coexistence of two types of hydrogen atoms in the same system makes $LaMg_2NiH_7$ a unique example system. Unfortunately, the hydrogenation reaction is not reversible under practical conditions.

Recently a similar metal-nonmetal transition is also reported in the palladium system $LaMg_2Pd$-H [63]. The intermetallic $LaMg_2Pd$ absorbs hydrogen under mild conditions (100∼200°C, 10 *bar*), forming nonmetallic hydride $LaMg_2PdH_7$. Full hydrogenation leads to the formation of tetrahedral $[PdH_4]^{4-}$ complexes, and the metal

host structure is nearly unchanged (metal atom shifts$\sim$0.7 Å) after hydrogenation. In contrast to the one-step hydrogenation of the nickel system, the hydrogenation of the palladium system $LaMg_2Pd$-H takes place in two steps:

$$2LaMg_2Pd + 3H_2 \rightarrow 2LaMg_2PdH_3 \quad (80)$$

$$LaMg_2PdH_3 + 2H_2 \leftrightarrow LaMg_2PdH_7 \quad (81)$$

The intermetallic $LaMg_2Pd$ first absorbs hydrogen to form low concentration hydride $LaMg_2PdH_3$, which further absorbs hydrogen to form full concentration hydride $LaMg_2PdH_7$. Unlike the nickel system, the hydrogenation of this system is partially reversible (step (81)), and therefore presents greater interest for applications.

5.2 Computational Details

Theoretical calculations are carried out using the Vienna ab-initio simulation package (VASP) [20] based on density functional theory [5] and the projector augmented wave method (PAW) [17] with plane waves. The generalized gradient approximation (GGA) [18] is used. The energy cutoff is 600 eV, and the k-point sampling grid is chosen so that the grid interval <0.2 Å^{-1} for the total-energy calculation and <0.1 Å^{-1} for the density of states calculations. The outer core shells ($5s$ and $5p$) of La are included as valence states.

5.3 Crystal Structures

Both hydrogen-free $LaMg_2Pd$ and low concentration hydride $LaMg_2PdH_3$ crystalize in orthorhombic space group Cmcm (No. 63), as shown in Figures 14 and 15. $LaMg_2Pd$ is in fact isostructural with its nickel analogue $LaMg_2Ni$. Interestingly, their fully hydrogenated compounds crystalize differently. While the nickel hydride $LaMg_2NiH_7$ crystallizes in centrosymmetric monoclinic symmetry, the full palladium hydride $LaMg_2PdH_7$ crystalizes in orthorhombic space group $P2_12_12_1$ (No. 19) (Figure 16). Of the seven hydrogen atoms, four are bonded to the palladium atom in a

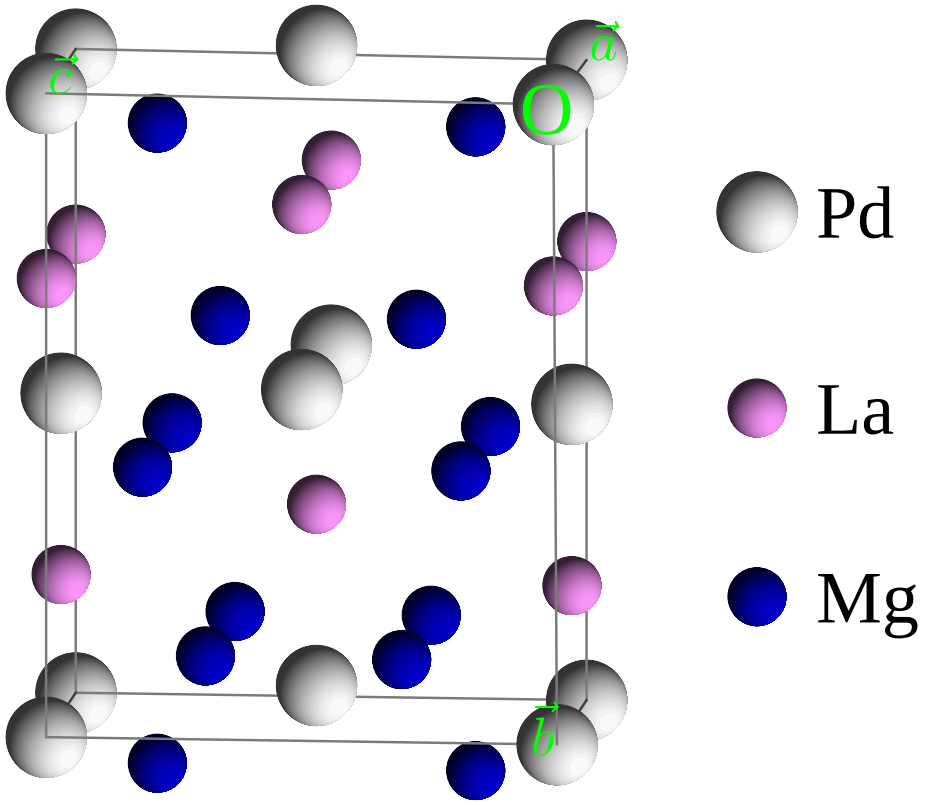

Figure 14: (Color online) Crystal structure of $LaMg_2Pd$. The large white spheres at the corner and semi-face-center positions stand for palladium atoms; the pink spheres stand for lanthanum atoms; and the blue spheres stand for magnesium atoms.

tetrahedral configuration forming the $[PdH_4]^{4-}$ complex, and three occupy La_2Mg_2-type tetrahedral interstices. The Pd-H bond distances are consistent with those in similar PdH_4-containing compounds such as M_2PdH_4, where M = Sr or Ba [64], and the H-Pd-H bond angles are comparable to those in the nickel analogue $LaMg_2NiH_7$. The nearest La-H and Mg-H distances are slightly shorter than those in the corresponding saline binary hydrides (LaH_3 and MgH_2). The metal-hydrogen bonds in $LaMg_2PdH_7$ are therefore expected to have a covalent (i.e., directional) character for palladium (presumably of sp^3-type) and an ionic (i.e., non-directional) character for lanthanum and magnesium. The hydride structure can be rationalized in terms of a palladium centered tetrahedral $[PdH_4]^{4-}$ complex having terminal hydrogen ligands ("complex" hydrogens), and hydrogen anions H^- surrounded by Mg^{2+} and La^{3+} cations only ("interstitial" hydrogens). This type of tetrahedral $[PdH_4]^{4-}$ complexes appear only in $LaMg_2PdH_7$ and M_2PdH_4, M = Sr or Ba. All other solid-state palladium-hydrogen complexes known are either linear complexes such as $[PdH_2]^{2-}$ in M_2PdH_2, M = Li or Na [65]; triangular complexes such as $[PdH_3]^{3-}$ in $NaBaPdH_3$ [66]; or square planar complexes such as $[PdH_4]^{2-}$ in Na_2PdH_4 [67, 68].

For the intermediate hydride $LaMg_2PdH_3$, three kinds of Wyckoff positions for H atoms are found, designated by H1, H2, and H3 (Figure 15). The experiment gives partial hydrogen occupancy on H1 and H2 sites, implying partially disordered structure with either H1 or H2 sites occupied. H1 and H3 sites are interstitial sites. Each H3 atom is surrounded by two Mg (Mg-H3$\sim$2.0 $\mathring{A}$) and two La (La-H3$\sim$2.4 $\mathring{A}$) atoms in a semi-tetrahedral configuration, and two neighboring H atoms on H3 chains along lattice vector $\vec{a}$ (H3-H3$\sim$2.3 and 2.4 $\mathring{A}$). Each H1 atom is surrounded by two Mg (Mg-H1$\sim$2.1 $\mathring{A}$) and two La (La-H1$\sim$2.5 $\mathring{A}$) atoms in a semi-tetrahedral configuration, and four in-plane H3 atoms (H1-H3$\sim$2.3 $\mathring{A}$). (Hydrogen atoms on H1 and H3 sites form layers perpendicular to lattice vector $\vec{b}$, the longest lattice vector.) H2 sites are ligand sites. Each H2 atom is close to one Pd atom (Pd-H2$\sim$1.8 $\mathring{A}$), and

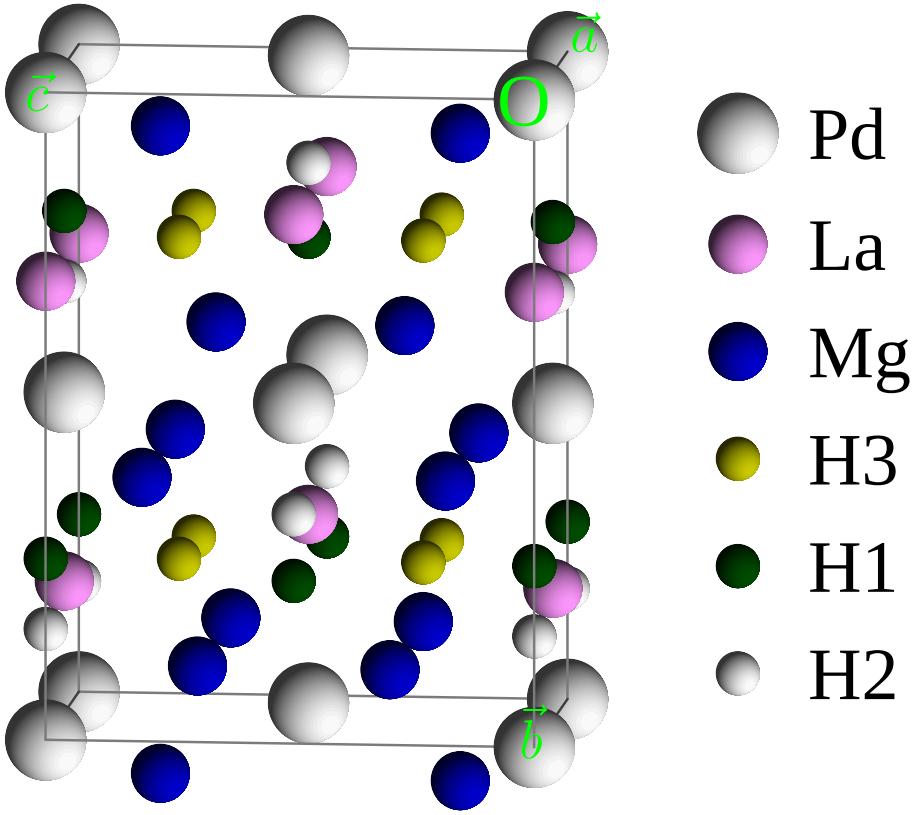

Figure 15: (Color online) Crystal structure of $LaMg_2PdH_3$, where partially disordered hydrogen arrangement is found with either Wyckoff position H1 (small dark-green spheres) or H2 (small white spheres) occupied. The large white spheres at the corner and semi-face-center positions stand for palladium atoms; the pink spheres stand for lanthanum atoms; the blue spheres stand for magnesium atoms; the small yellow-greenish spheres stand for hydrogen atoms at Wyckoff position H3.

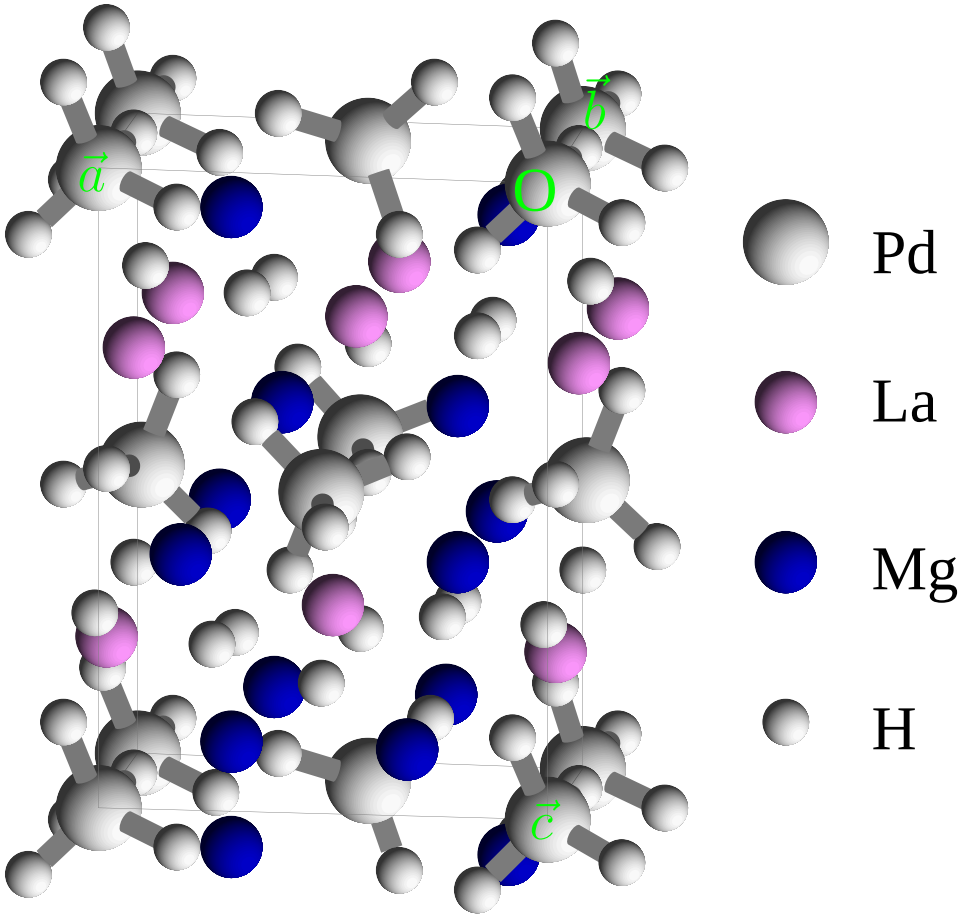

Figure 16: (Color online) Crystal structure of $LaMg_2PdH_7$. The large white spheres at the corner and semi-face-center positions stand for palladium atoms; the pink spheres stand for lanthanum atoms; the blue spheres stand for magnesium atoms; and the small white spheres stand for hydrogen atoms. The hydride structure can be described as consisting of palladium-centered tetrahedral $[PdH_4]^{4-}$ complexes each having 4 terminal hydrogen ligands ("complex" hydrogens) and hydrogen anions H^- surrounded by Mg^{2+} and La^{3+} cations only ("interstitial" hydrogens).

Table 7: Experimental lattice parameters of $LaMg_2PdH_x$, x=0, 3, 7. All 3 compounds crystalize in orthorhombic lattices.

	symmetry group	experimental lattice constants ($\AA$)			volume ($\AA^3$/f.u.)
$LaMg_2Pd$	Cmcm	4.3228	8.3095	10.5289	94.55
$LaMg_2PdH_3$	Cmcm	4.7526	7.9765	10.6451	100.89
$LaMg_2PdH_7$	$P2_12_12_1$	4.7745	8.1036	11.7160	113.32

is surrounded by two La (La-H1$\sim$2.4 $\AA$) and two Mg (Mg-H1$\sim$2.5 $\AA$) atoms in an almost "flat" tetragonal configuration. One H2 and four H3 (H2-H3$\sim$2.5 $\AA$) atoms form a flat pyramid (with the H2 atom as the vertex).

A close connection exists [62] between the structures of the low concentration hydride $LaMg_2PdH_3$ and the full hydrogenated $LaMg_2PdH_7$, as shown in Figures 15 and 16. Wyckoff positions H1/H3 in $LaMg_2PdH_3$ correspond to interstitial hydrogen sites Hi2/(Hi1+Hi3) in $LaMg_2PdH_7$ with a shorter Pd-H distance; Wyckoff positions H2 in $LaMg_2PdH_3$ correspond to ligand hydrogen sites Hl1 in $LaMg_2PdH_7$ (Pd-Hl1$\sim$1.7 $\AA$) with a longer Pd-H distance. The difference between ligand and interstitial Pd-H distances is not as big in $LaMg_2PdH_3$ as in $LaMg_2PdH_7$. In $LaMg_2PdH_3$, due to the partial occupancy of either H1 or H2 sites, the corresponding distance between these two sites is much closer ($\sim$1.15 $\AA$) than in $LaMg_2PdH_7$ (Hi2-Hl1$\sim$2.1 $\AA$) where both sites are occupied simultaneously. Part of Hi2 and of Hl1, together with the other three ligand hydrogen atoms Hl2-Hl4, are lost during dehydrogenation of $LaMg_2PdH_7$ to form $LaMg_2PdH_3$.

Table 7 lists lattice parameters of the $LaMg_2PdH_x$ system. Hydrogenation induces a decrease in symmetry, i.e., from centrosymmetric to non-centrosymmetric. The cell volume expands with increasing hydrogen content. The increase in cell volume is $\sim$20% from the intermetallic to the fully hydrogenated state and $\sim$12% from the low hydrogen concentration state to the fully hydrogenated state. From $LaMg_2PdH_3$ to $LaMg_2PdH_7$, the biggest change ($\sim$10%) in cell dimension is in the longest lattice

constant due to the insertion of ligand hydrogen atoms (and the formation of the PdH_4 complex).

5.4 Energetics and Electronic Structures

The full occupancy of H1 or H2 sites is considered separately for $LaMg_2PdH_3$. Total energy calculations give the configuration with an H2 occupancy as the lowest energy configuration. Calculated total energy for the configuration with an H2 occupancy is 0.026 eV (per formula unit) lower than that with an H1 occupancy. The reaction enthalpy (approximated as the difference in total energy of products and reactants) is -41 kJ/mol-H_2 according to Equation (81), comparable with the desorption enthalpy estimated from the PCT data [63].

Calculations on the band structure (not shown) reveal no band gap for $LaMg_2Pd$ and $LaMg_2PdH_3$, and a fundamental direct gap of 0.7 eV at Γ (GGA result) for $LaMg_2PdH_7$. The real gap is estimated to be more than 1.0 eV. Metal-nonmetal transition does not happen immediately upon hydrogenation of intermetallic $LaMg_2Pd$; rather it happens from the low concentration hydride $LaMg_2PdH_3$ to the full concentration hydride $LaMg_2PdH_7$.

This can be confirmed in the projected density of states (PDOS) plots for $LaMg_2Pd$, $LaMg_2PdH_3$, and $LaMg_2PdH_7$, as shown in Figures 17, 18, 19, and 20. Energy zero is set at the Fermi level. The projection radii used were 1.5 $\mathring{A}$ for La, 1 $\mathring{A}$ for Mg, 1.2 $\mathring{A}$ for Pd, and 0.8 $\mathring{A}$ for H. These PDOS plots represent a sum over the various atomic sites for a single element (or a single kind of Wyckoff position in the case of H1 or H2 occupancy in $LaMg_2PdH_3$). There is no contribution from orbitals of Mg, La *spd*, and Pd *spf* in the energy range of interest. An examination of the charge density (not shown) concludes that magnesium behaves like an electron donor with very little valence charge in its vicinity. Hydrogen attracts charge as expected from its relatively large electronegativity.

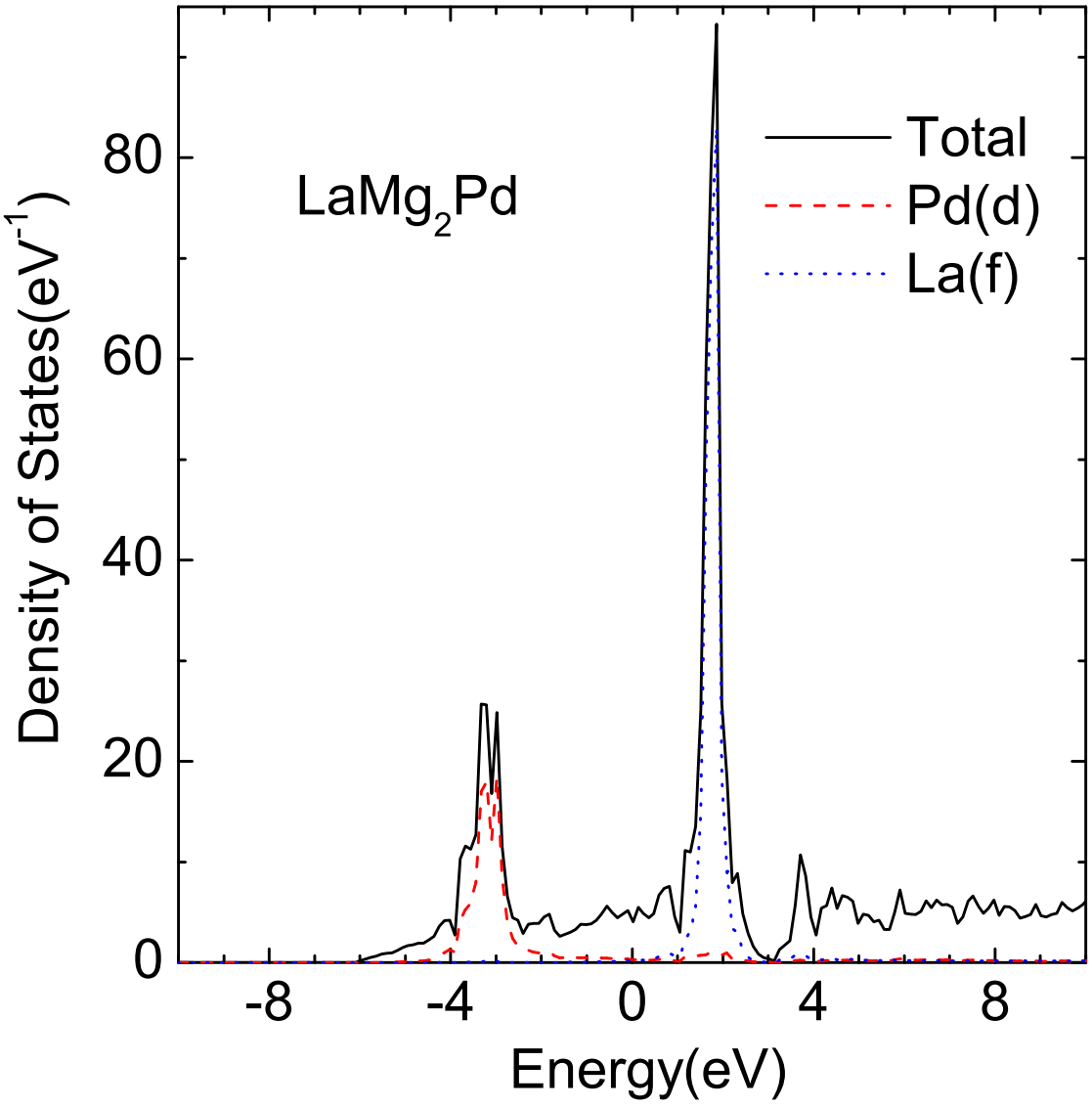

Figure 17: (Color online) Density of states of $LaMg_2Pd$: Total density of states, and projected density of states for Pd d and La f.

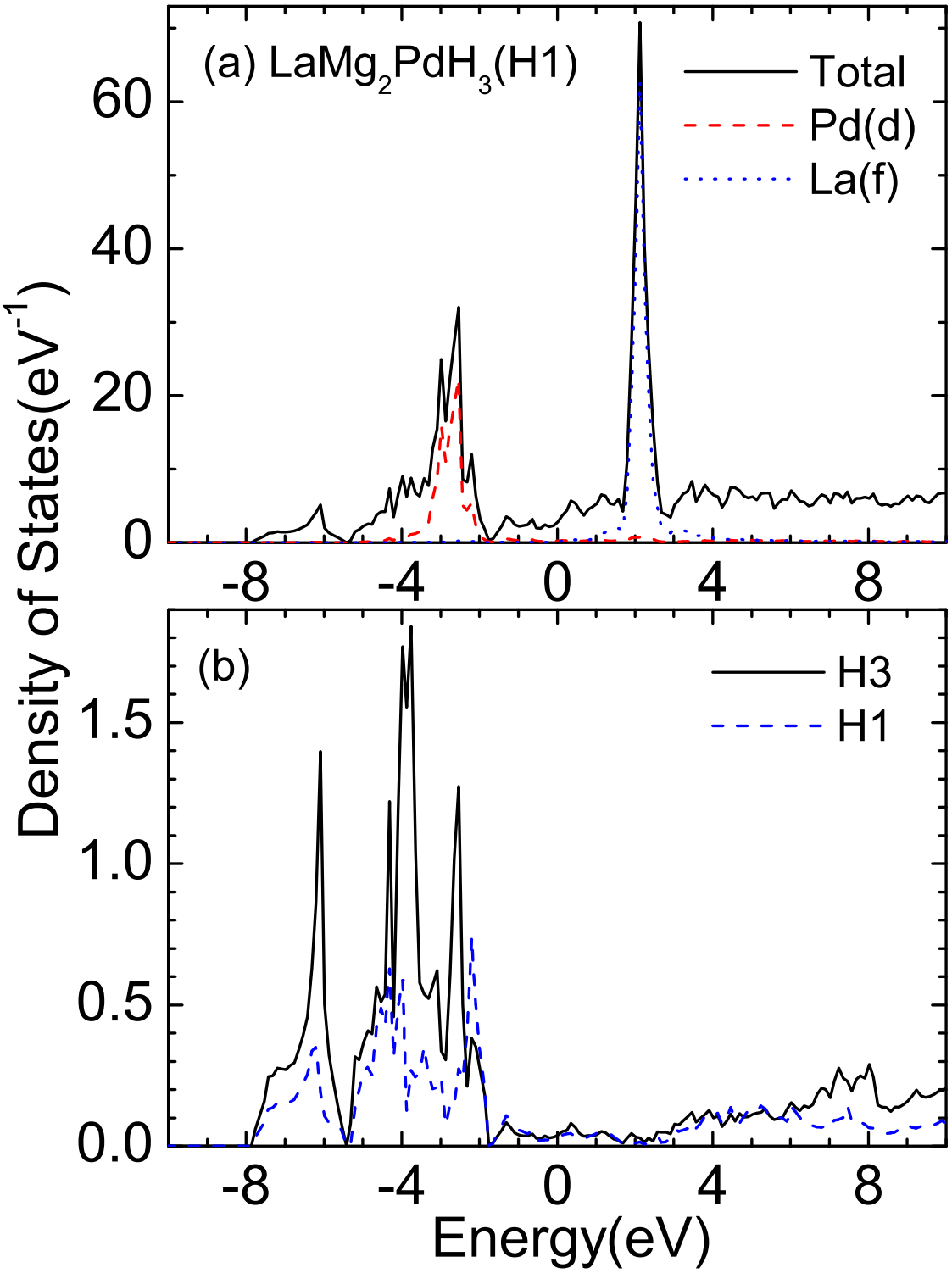

Figure 18: (Color online) Density of states of $LaMg_2PdH_3$ with an H1 occupancy: (a) Total density of states, and projected density of states for Pd d and La f; (b) Projected density of states for H1 and H3.

In all cases the La f bands form a peak around +2 eV in the conduction band (unoccupied), while the Pd d bands form a main peak around -3 eV in the valence band. In the intermetallic $LaMg_2Pd$ (and $LaMg_2PdH_3$ with an H1 occupancy), this is the only Pd d peak, indicating no significant local electronic interaction of Pd with other atoms. In $LaMg_2PdH_3$ with an H2 occupancy, this main peak starts to have small satellite peaks on both sides. Positions of these Pd d side peaks coincide with some of the H s peaks, indicating onset of local electronic interaction between Pd and H. A check of the band-projected partial charge density shows that the peak on the low (high) energy side corresponds to the bonding (anti-bonding) interaction between Pd and ligand H.

In $LaMg_2PdH_7$, the projected density of states for Pd d further spreads out over the whole range of -8 to 0 eV and overlaps with that of H s in the low energy range of -6 to -4.5 eV. Almost all the Pd d states are below the gap, indicating an approximately closed d shell. One can identify three broad groups of peaks in the projected density of states associated with hydrogen. They can be associated with states (in the order of rising energy) from H s in the complex, H s interstitial, and (a small peak from) H s in the complex, respectively. The first group corresponds to Pd-H bonding states (-7 to -5 eV), which is higher in intensity than the third group that corresponds to the Pd-H anti-bonding states (-2 to 0 eV), resulting in overall stable PdH_4 complex configuration (in agreement with the 18-electron full shell model given by sp^3 hybridization scheme). There is little overlap between the spectra of these two kinds of hydrogen atoms (except the peak around -4.7 eV). As mentioned above, the structure of the fully hydrogenated compound can be described in terms of palladium centered tetrahedral $[PdH_4]^{4-}$ complexes each having four ligand complex hydrogens, and interstitial hydrogen anions H^- surrounded only by Mg^{2+} and La^{3+} cations. The chemical formula then can be written in the limiting ionic form of $LaMg_2PdH_7$=$La^{3+}2Mg^{2+}[PdH_4]^{4-}\cdot 3H^-$. The $[PdH_4]^{4-}$ complex conforms to

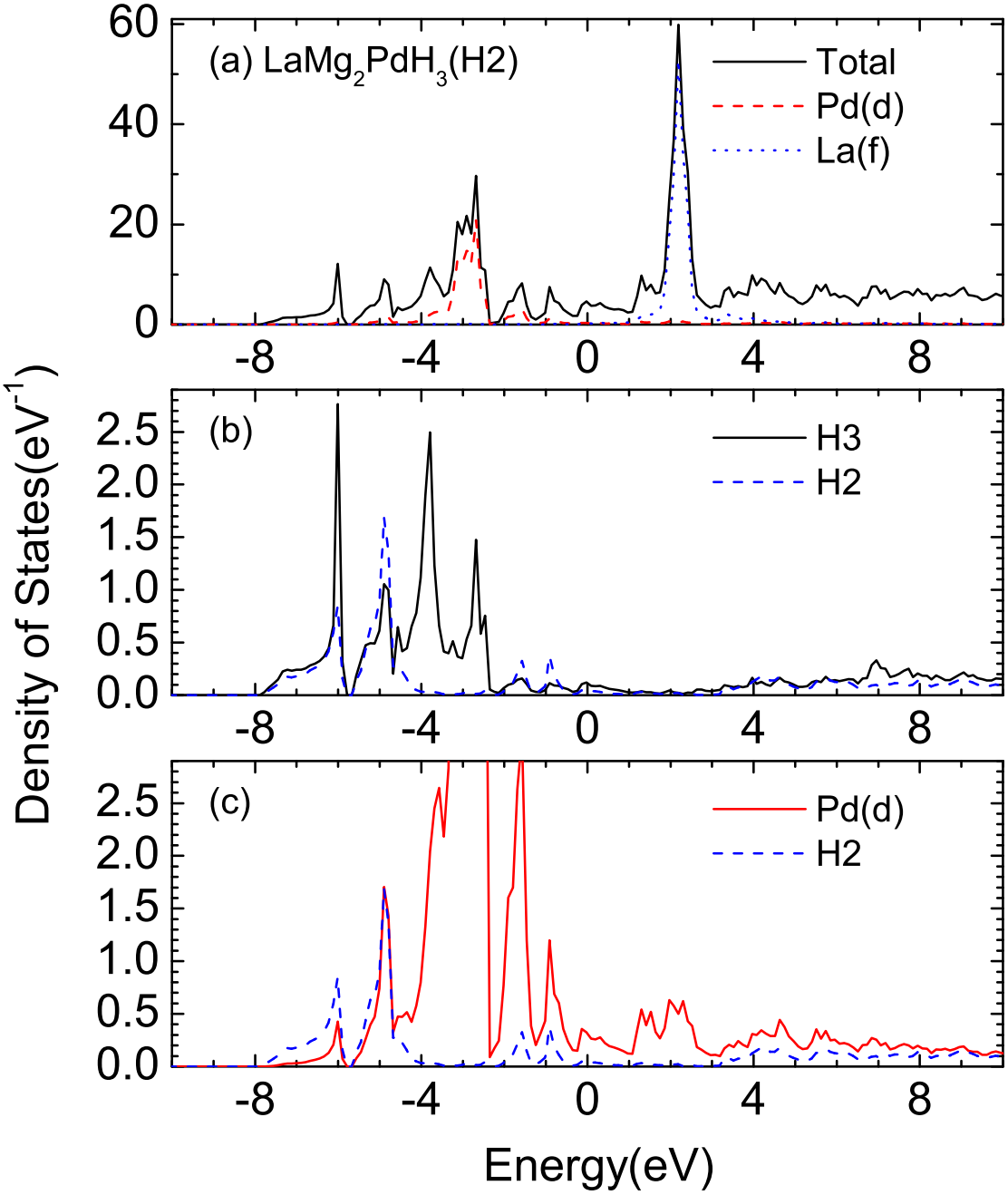

Figure 19: (Color online) Density of states of $LaMg_2PdH_3$ with an H2 occupancy: (a) Total density of states, and projected density of states for Pd d and La f; (b) Projected density of states for H2 and H3; and (c) Projected density of states for Pd d and H2 (to show the detailed overlap between the two).

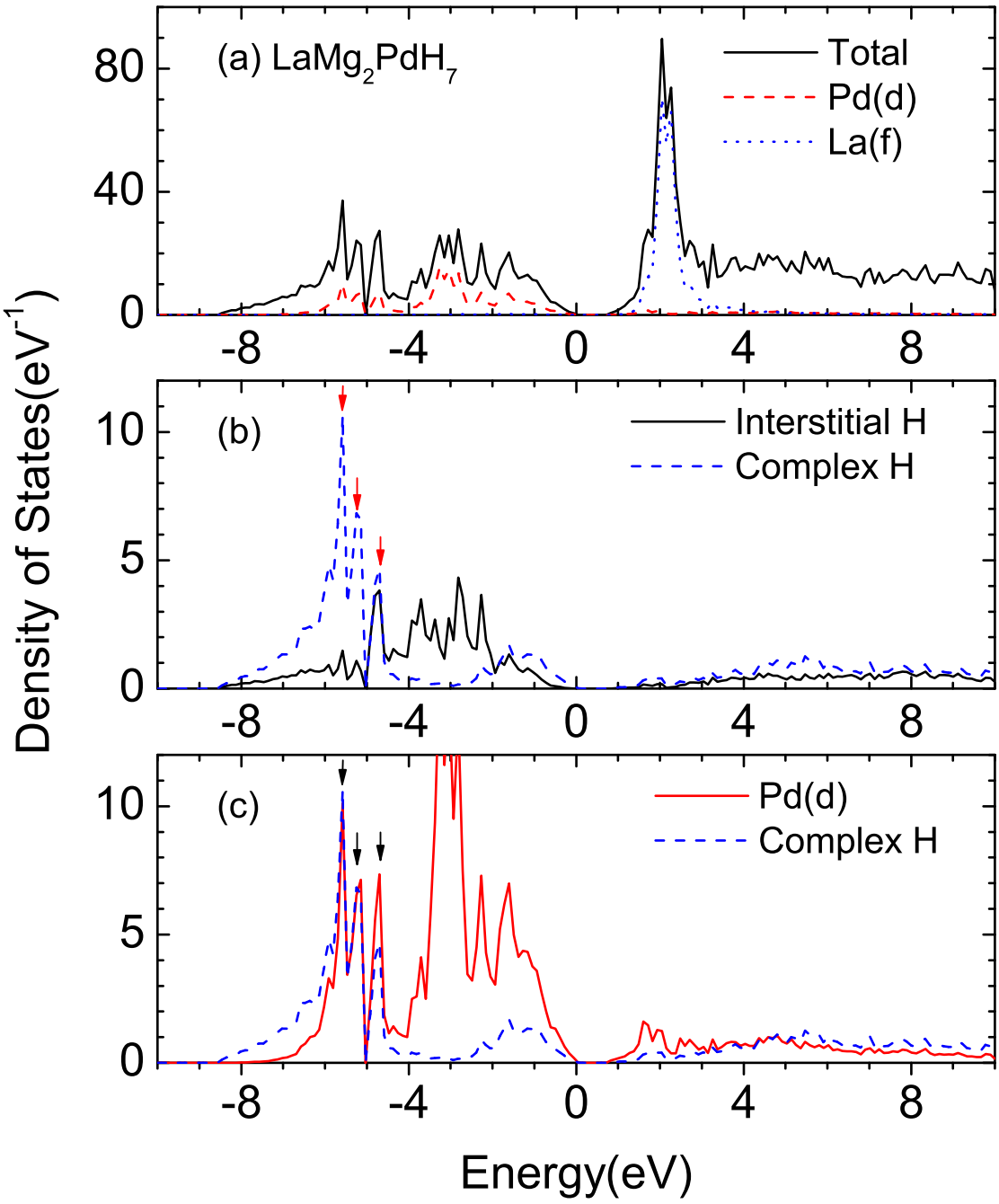

Figure 20: (Color online) Density of states of $LaMg_2PdH_7$: (a) Total density of states, and projected density of states for Pd d and La f; (b) Projected density of states for interstitial and complex hydrogen; and (c) Projected density of states for Pd d and complex hydrogen. The positions of the three peaks marked by arrows in (b) and (c) are at -5.58, -5.14, and -4.70 eV, respectively. As shown in (c), the two peaks in the lower energy range are uniquely for Pd d and complex H s, and represent electronic interaction within the PdH_4 complex.

the 18-electron rule. In other words, the Pd atom is zero-valent and has an electronic configuration of d^{10}. This implies a charge transfer from La and Mg atoms to both the complex and the intersitial hydrogen atoms, so that the Pd d bands are nearly filled and all valence electrons are localized in metal-hydrogen bonds, rendering the hydride non-metallic.

In the projected density of states plots for $LaMg_2PdH_3$ with an H1 or H2 occupancy, the broad peaks associated with H1 or H3 span the whole energy range of -8 to 0 eV, exhibiting the same characteristics as that of interstitial hydrogen in $LaMg_2PdH_7$. In the projected density of states plot for $LaMg_2PdH_3$ with an H2 occupancy, the H2 spectrum below zero is made up by two groups of peaks in the range of -8 to -4 eV and -2 to 0 eV, respectively, exhibiting the same characteristics as that of complex hydrogen in $LaMg_2PdH_7$. Overall the projected density of states of "complex" hydrogen is located at a lower energy range than that of "interstitial" hydrogen. This explains the decrease in the total energy for $LaMg_2PdH_3$ with an H2 occupancy.

Compared with the fully hydrogenated state, there is a single common peak (around -6.1 eV) associated with H1 and H3 in the low energy range (-8∼-5.4 eV) for $LaMg_2PdH_3$ with an H1 occupancy. For $LaMg_2PdH_3$ with an H2 occupancy, this peak contains states associated with H2, H3, and Pd d, with a narrowed range (-8∼-5.8 eV) and an increased peak intensity. There is also a second common peak (at -4.9 eV) associated with H2, H3, and Pd d. As discussed before, the H1 and H2 sites are just 1.15 $\mathring{A}$ apart, and H2 is ligand to one palladium atom.

In order to compare the detailed nature of the Pd-H bonding in these two cases, we calculated the band projected partial charge density at the Γ point. The calculation is done for bands with energies ranging from -8.00 to -4.04, and -2.76 to -0.25 eV for $LaMg_2PdH_3$ with an H1 occupancy; and from -8.00 to -4.00, and -2.93 to 0.65 eV for $LaMg_2PdH_3$ with an H2 occupancy. Figure 21 shows contour plots of partial

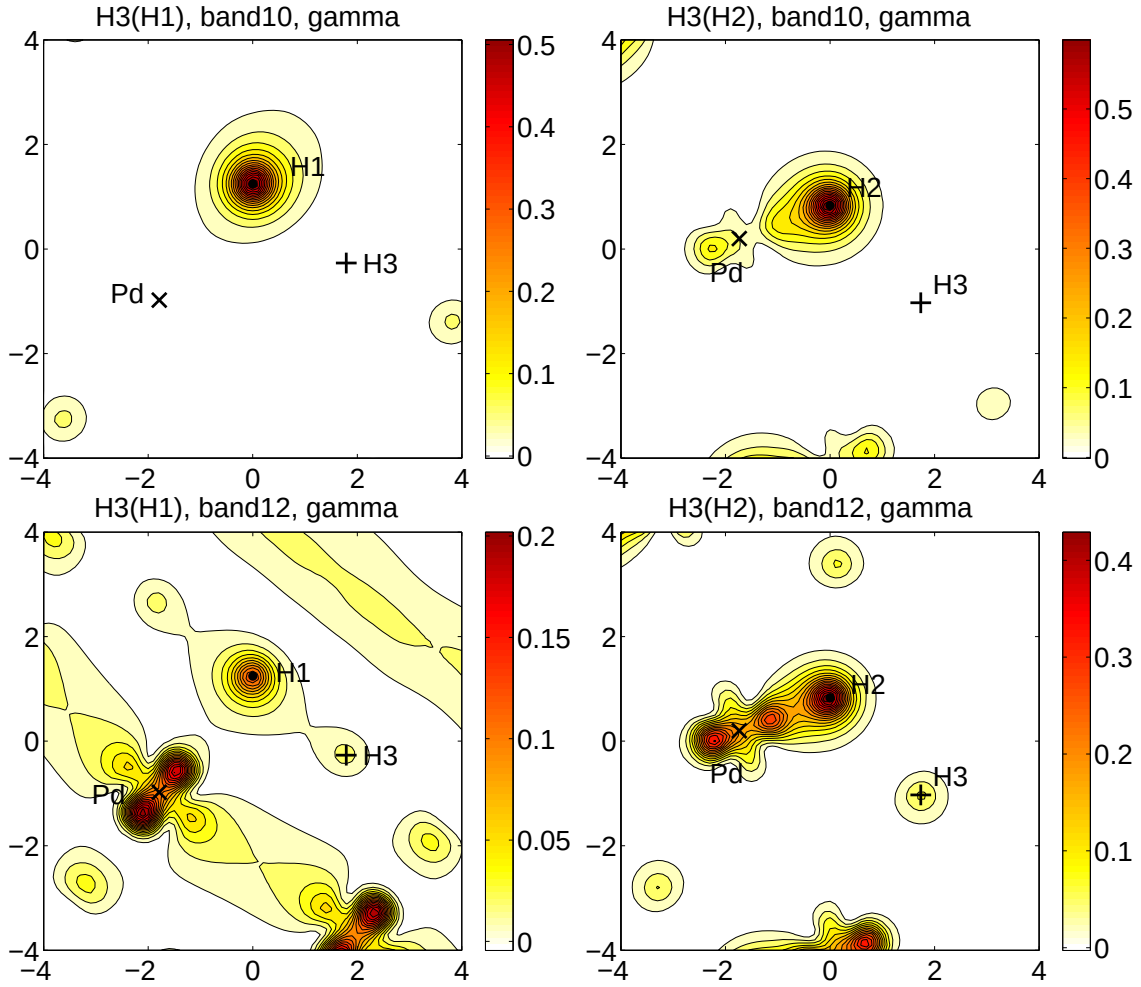

Figure 21: (Color online) Band projected partial charge density plot at Γ. The plot is for a plane (8×8, in $\mathring{A}$) containing Pd (×), H1 (or H2) (•), and H3 (+) atoms. H2 occupancy (right) shows significant interaction between Pd and ligand H2, while H1 occupancy (left) shows no such interaction.

charge density for a couple of selected bands. The plots are for a plane (8 Å by 8 Å in dimension) containing one Pd, one H1 (or H2), and one H3 atoms. Plots on the left side are for $LaMg_2PdH_3$ with an H1 occupancy, where the top and bottom plots are for band number 10 (with a band energy of -5.68 eV) and band number 12 (with a band energy of -4.08 eV), respectively. Plots on the right side are for $LaMg_2PdH_3$ with an H2 occupancy, where the top and bottom plots are for band number 10 (with a band energy of -6.27 eV) and band number 12 (with a band energy of -5.05 eV), respectively. From these plots, it is clear that in $LaMg_2PdH_3$ with an H2 occupancy, there is a significant sharing of electrons between Pd and H2 atoms, indicating direct bonding of Pd-H2. On the other hand, this Pd-H bonding is absent between Pd and H1 atoms in $LaMg_2PdH_3$ with an H1 occupancy.

5.5 Summary

To summarize, analogous to the $LaMg_2Ni$-H system, hydrogenation-induced metal-nonmetal transition occurs in the quaternary transition-metal-hydrogen system $LaMg_2Pd$-H. In contrast to the nickel system, the hydrogenation takes place in two steps, and is partially reversible under technically useful conditions. For the low concentration hydride $LaMg_2PdH_3$, experiment gives a disordered occupancy of certain hydrogen sites, and the exact position of the hydrogen atoms in this intermediate phase is not determined.

Theoretical calculations were carried out based on density functional theory and the projector augmented wave method (PAW) with plane waves. The energetics of the $LaMg_2Pd$-H system is examined through total energy calculations. The band structure and density of states are calculated for the intermetallic $LaMg_2Pd$, low concentration hydride $LaMg_2PdH_3$, and full hydrogenated compound $LaMg_2PdH_7$. The partial charge density for certain bands is calculated and compared in configurations of $LaMg_2PdH_3$ with a full H1 or H2 occupancy. Our first-principles calculation

shows the metal-nonmetal transition happens from the low concentration hydride $LaMg_2PdH_3$ to the terminal hydride $LaMg_2PdH_7$. For $LaMg_2PdH_3$, the configuration with a full occupancy of H2 sites is 0.026 eV (per formula unit) lower in energy than that with a full occupancy of H1 sites, which can be explained by the ligand interaction of the H2 atom with the nearest palladium atom. In terminal hydride $LaMg_2PdH_7$, this interaction of the Pd d and ligand H s orbitals within the PdH_4 complex is further strengthened, leading to an even more dispersed Pd d spectrum toward the lower energy range in the projected density of states plot, which eventually results in an energy gap. This is in agreement with the 18-electron full shell model of the $[PdH_4]^{4-}$ complex.

REFERENCES

[1] E. Fermi, Un Metodo statistico per la determinazione di alcume priorieta dell'atome, Rend. Accad. Naz. Lincei **6**, 602(1927).

[2] M. S. Dresselhaus and I. L. Thomas, Nature **414**, 332(2001).

[3] For example, see A. Zuttel, Materials Today **6**(9), 24(2003); L. Schlapbach and A. Zuttel, Nature **414**, 353(2001).

[4] J. A. Ritter, A. D. Ebner, J. Wang, and R. Zidan, Materials Today **6**(9), 18(2003).

[5] P. Hohenberg and W. Kohn, Phys. Rev. **136**, B864(1964); W. Kohn and L.J. Sham, *ibid.* **14 0**, A1133(1965).

[6] G. Sandrock, IEA, task 17 http://hydpark.ca.sandia.gov/iea.html

[7] J. Ihm, A. Zunger, and M. L. Cohen, J. Phys. C, **12**, 4409(1979).

[8] J. C. Philips and L. Kleinman, Phys. Rev. **116**, 287(1959).

[9] L. Kleinman and J. C. Philips, Phys. Rev. **118**, 1153(1960).

[10] M. H. Cohen and V. Heine, Phys. Rev. **122**, 1821(1961).

[11] B. J. Austin, V. Heine, and L. J. Sham, Phys. Rev. **127**, 276(1962).

[12] D. R. Hamann, M. Schlüter, and C. Chiang, Phys. Rev. Lett. **43**, 1494(1979).

[13] N. Troullier and J. L. Martins, Phys. Rev. B **43**, 1993(1991).

[14] L. Kleinman and D. M. Bylander, Phys. Rev. Lett. **48**, 1425(1982).

[15] D. Vanderbilt, Phys. Rev. B **41**, 7892(1990).

[16] K. Laasonen, R. Car, C. Lee, and D. Vanderbilt, Phys. Rev. B **43**, 6796(1991).

[17] P.E. Blöchl, Phys. Rev. B **50**, 17953(1994).

[18] J. P. Perdew and Y. wang, Phys. Rev. Lett. **66**, 508(1991); J. P. Perdew, K. burke, and M. Ernzerhof, Phys. Rev. Lett. **77**, 3865(1996).

[19] V. P. Balema, K. W. Dennis, and V. K. Pecharsky, Chemical Communications **17**, 1655(2000)

[20] G. Kresse and J. Furthmüller, Comput. Mat. Sci. **6**, 15(1996); G. Kresse and J. Furthmülle r, Phys. Rev. B **54**, 11169(1996).

[21] R. T. Walters and J. H. Scogin, J. Alloys Compd. **421**, 54(2006).

[22] B. Bogdanovic and M. Schwickardi, J. Alloys Compd. **253-254**, 1(1997).

[23] For example, see L. Zaluski, A. Zaluska, and J. O. Ström-Olsen, J. Alloys Compd. **290**, 71(1999).

[24] A. Peles, J. A. Alford, Z. Ma, L. Yang, and M. Y. Chou, Phys. Rev. B **70**, 165105(2004).

[25] P. Vajeeston, P. Ravindran, R. Vidya, H. Fjellvåg, and A. Kjekshus, Phys. Rev. B **68**, 212101(2003).

[26] B.C. Hauback, H.W. Brinks, C.M. Jensen, K. Murphy, and A.J.Maeland, J. Alloys Compd. **358**. 142(2003).

[27] B. C. Hauback, H. W. Brinks, and H. Fjellvåg, J. Alloys Compd. **346**, 184(2002).

[28] A. Fossdal, H. W. Brinks, M. Fichtner, and B. C. Hauback, J. Alloys Compd. **387**, 47(2005).

[29] E. Rönnebro, D. Noréus, K. Kadir, A. Reiser, and B. Bogdanovic, J. Alloys Compd. **299**, 101(2000).

[30] H. W. Brinks, B. C. Hauback, C. M. Jensen, and R. Zidan, J. Alloys Compd. **392**, 27(2005); J. Graetz, Y. Lee, J. J. Reilly, S. Park, and T. Vogt, Phys. Rev. B **71**, 184115(2005).

[31] H. W. Brinks and B. C. Hauback, J. Alloys Compd. **354**, 143(2003).

[32] M. E. Arroyo y de Dompablo and G. Ceder, J. Alloys Compd. **364**, 6(2004).

[33] O. M. Lovvik and O. Swang, Europhys. Lett. **67**, 607(2004).

[34] P. Chen, Z. Xiong, J. Luo, J. Lin, and K. L. Tan, Nature **420**, 302(2002).

[35] P. Chen, Z. Xiong, J. Luo, J. Lin, and K. L. Tan, J. Phys. Chem. **107**, 10967(2003).

[36] Z. Xiong, P. Chen, G. Wu, J. Lin, K. L. Tan, J. Mater. Chem. **13**, 1676(2003).

[37] T. Ichikawa, S. Isobe, N. Hanada, and H. Fujii, J. Alloys Compd. **365**, 271(2004).

[38] Z. Xiong, G. Wu, J. Hu, and P. Chen, Adv. Mater. **16**(17), 1522(2004).

[39] Z. Xiong, J. Hu, G. Wu, and P. Chen, J. Alloys Compd. **395**, 209(2005).

[40] Z. Xiong, J. Hu, G. Wu, P. Chen, W. Luo, K. Gross, and J. Wang, J. Alloys Compd. **398**, 235(2005).

[41] Z. Xiong, G. Wu, J. Hu, P. Chen, W. Luo, and J. Wang, J. Alloys Compd. **417**, 190(2006).

[42] F. Pinkerton, G. Meisner, M. Meyer, M. Balogh, and M. Kundrat, J.Phys. Chem. B **109**, 6(2005).

[43] Y. Nakamori and S. Orimo, Mater. Sci. Eng. B **108**, 48(2004).

[44] Y. Nakamori and S. Orimo, J. Alloys Compd. **370**, 271(2004).

[45] Y. Nakamorii, G. Kitahara, and S. Orimo, J. Power Sources **138**, 309(2004).

[46] Y. Nakamori, T. Yamagishi, M. Yokoyama, and S. Orimo, J. Alloys Compd. **377**, L1(2004).

[47] Y. Nakamori, G. Kitahara, K. Miwa, S. Towata, and S. Orimo, Appl. Phys. A **80**, 1(2005).

[48] W. Luo, J. Alloys Compd. **381**, 284(2004).

[49] W. Luo and E. Rönnebro, J. Alloys Compd. **404-406**, 392(2005).

[50] W. Luo and S. Sickafoose, J. Alloys Compd. **407**, 274(2006).

[51] H. Leng, T. Ichikawa, S. Hino, N. Hanada, S. Isobe, and H. Fujii, J.Phys. Chem. B **108**,8763(2004).

[52] T. Ichikawa, K. Tokoyoda, H. Leng, and H. Fujii, J. Alloys Compd. **400**, 245(2005).

[53] H. Leng, T. Ichikawa, and H. Fujii, J.Phys. Chem. B **110**, 12964(2006).

[54] S. V. Alapati, J. K. Johnson, and D. S. Sholl, J. Phys. Chem. B, **110**, 8769(2006).

[55] J. Rijssenbeek, Y. Gao, J. C. Hanson, Q. Huang, C. Jones, and B. H. Toby, in press.

[56] M. P. Balogh, C. Y. Jones, J. F. Herbst, L. G. Hector Jr., and M. Kundrat, J. Alloys Compd. **420**, 326(2006).

[57] J. Yang, A. Sudik, C. Wolverton, J. Alloys Compd. in press(2006).

[58] J. Ihm, A. Zunger, & M. L. Cohen, J. Phys. C, **12**, 4409(1979).

[59] R. D. Shannon, Acta Crystallogr. **A32**, 751(1976).

[60] G. Renaudin, L. Guénée, and K. Yvon, J. Alloys Compd. **350**, 145(2003).

[61] K. Yvon, G. Renaudin, C. M. Wei, and M. Y. Chou, Phys. Rev. Lett. **94**, 066403(2005).

[62] For orthorhombic cell(Z=4), position one of the Pd atoms at origin, and make the correspondence between lattice vectors of $LaMg_2PdH_7$ and $LaMg_2PdH_3$ as: $\vec{a} \leftrightarrow \vec{c}$, $\vec{b} \leftrightarrow \vec{a}$, $\vec{c} \leftrightarrow \vec{b}$.

[63] K. Yvon, J.-Ph. Papin, N. Penin, Z. Ma, and M. Y. Chou, J. Alloys Compd. **446-447**, 34(2007).

[64] M. Olofsson-Mårtensson, M. Kritikos, and D. Noréus, J. Am. Chem. Soc. **121**, 10908(1999).

[65] D. Noréus, H. Spittank, A. Börge, and T. Szabo, J. Less Common Met. **139**, 233(1988).

[66] M. Olofson, M. Kritikos, and D. Noréus, Inorg. Chem. **37**, 2900(1988).

[67] W. Bronger and G. Auffermann, J. Alloys Compd. **228**, 119(1995).

[68] K. Yvon and G. Renaudin, in: R. B. King(Ed.), Hydrides: Solid State Transition Metal Complexes, 2nd ed., John Wiley & Sons Ltd., 2005, ISBN 0-470-86078-2, pp. 1814-1846.

VITA

Zhu Ma was born on November 30th, 1974 in Guanyu town, city of Deyang, Sichuan Province, China. She has a mother who teaches maths, a father who teaches English. Both retired now, her father still loves fishing, and her mother has Hyperlipidemia. She has an elder brother, a sister-in-law, and an 8-year nephew. Now with her husband she has her own lovely child, James.

She was enrolled in the department of Physics at Beijing Normal University in 1994 and received her B.S. in 1998. Graduated with honor, she was recommended to enter the graduate program there. She worked on analytical study of surface and interface and received her M.S. in 2001. In the same year, she came to U.S.A. to continue her graduate study at School of Physics, Georgia Institute of Technology. Since then she has concentrated her Phd work on the first-principles study of hydrogen storage materials.